

# **GROWTH AND PHYSICAL PROPERTIES OF COBALT- DOPED n-TYPE ZnO THIN FILMS SYNTHESIZED WITH PULSED LASER ABLATION**

*A thesis submitted*

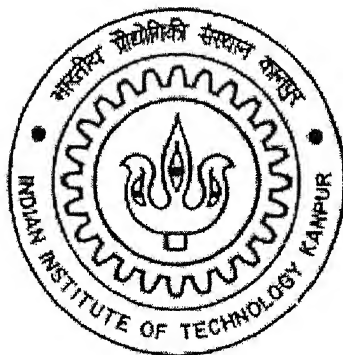
In Partial Fulfillment of the Requirements

for the Degree of

**Master of Technology**

by

**Prita Pant**



**MATERIALS SCIENCE PROGRAMME**

**INDIAN INSTITUTE OF TECHNOLOGY, KANPUR**

**July, 2004**

21 OCT 2004

मुख्योत्तम गोपीनाथ केलकर पुस्तकालय

भारतीय प्रोद्योगिकी संस्थान कानपुर

पचासि क्र० A...149266-----

TH

MSP/2004/M

P19542



A149266



## CERTIFICATE

It is certified that the work contained in the thesis entitled **“Growth and Physical Properties of Cobalt-doped n-type ZnO Thin Films synthesized with Pulsed Laser Ablation”** by Prita Pant has been carried out under our supervision and this work has not been submitted elsewhere for a degree.

Jitendra Kumar

(Jitendra Kumar)  
Professor  
Materials Science Programme  
Indian Institute of Technology Kanpur  
Kanpur – 208016

R. C. Budhani

(R. C. Budhani)  
Professor  
Department of Physics  
Indian Institute of Technology Kanpur  
Kanpur – 208016

## ABSTRACT

Dilute Magnetic Semiconductors (DMS) have attracted considerable attention in recent years due to their spin functionality. These materials are important for the realization of future “Spintronic” devices. The focus of our study is a II-VI DMS: n-type ZnO doped with cobalt with the general formula:

$(\text{Zn}_{1-x}\text{Co}_x\text{O})_{99}(\text{Al}_2\text{O}_3)_1$  with  $x = 0, 0.05, 0.10, 0.20, 0.25$  and  $0.30$

It has been synthesized and studied in bulk as well as thin film forms.

Polycrystalline samples have been synthesized in the form of small pellets using ceramic processing route. For thin films, we have used the technique of Pulsed Laser Ablation. Structural analysis yields a maximum solubility of 20 percent of  $\text{Co}^{2+}$  in the ZnO lattice at room temperature for both the forms. Electron microscopy of bulk samples provides no evidence for Co clustering even for  $x = 0.30$ . Magnetic characterization of bulk samples show that they are paramagnetic with an antiferromagnetic interaction between the nearest  $\text{Co}^{2+}$  ions. The films are highly transparent (~90%) in the visible regime with certain absorption bands appearing around ~2 eV. The optical band edge shows a red shift with increased Co doping. The resistivity of the films is few mohm-cm and the samples become increasingly resistive with Co doping. The carrier concentration and the Hall mobility are suppressed with Co incorporation. Magnetic state for thin films is paramagnetic for  $x = 0.10$  and superparamagnetic for  $x = 0.20$  and  $0.30$  with blocking temperature ( $T_B$ ) as high as ~300K. These two compositions have also shown clear signs of hysteresis at 10K although with negligible remnant magnetization, which further supports a superparamagnetic state. The interaction between the nearest  $\text{Co}^{2+}$  ions is found to be antiferromagnetic in the films as well.

## ACKNOWLEDGEMENT

I express my deep gratitude towards my guides, Prof. R. C. Budhani and Prof. Jitendra Kumar, for their able guidance and constant encouragement throughout the duration of this project.

I extend my sincere thanks to all my friends in both the labs, especially to my seniors, Navneet, Rajib and Kartik. Their help and support has been vital in the completion of this work.

I would also like to express my thanks to Rajeev, Thapaji, Sushant, Uma Shankarji and Barthwalji for help during the experiments.

Finally, I am thankful to my parents and sister for their moral support, and for the absolute faith they bestow on me.

# CONTENTS

Abstract	(iii)
Acknowledgement	(iv)
List of Figures	(vii)

## 1. INTRODUCTION

1.1 Background.....	1
1.2 Making Of A DMS.....	2
1.3 Motivation For The Present Work.....	4
1.4 Structural Properties.....	5
1.5 Electron Microscopy.....	7
1.6 Optical Properties.....	8
1.7 Transport Properties.....	9
1.8 Magnetic Properties.....	9
1.9 Highlights Of The Present Work.....	11

## 2. THIN FILM FABRICATION & CHARACTERIZATION TECHNIQUES

2.1 Introduction.....	13
PART A:	
2.2 Preparation of thin film and bulk samples.....	13
2.2.1 Target preparation.....	14
2.2.2 Thin film fabrication.....	14
2.2.2(a) Technique of pulsed laser deposition.....	14
2.2.2(b) Excimer laser.....	16
2.2.2(c) Vacuum chamber.....	17
2.2.2(d) Experimental setup and deposition conditions.....	17
PART B:	
2.3 Measurements of structure and properties.....	19
2.3.1 X- ray diffraction using a diffractometer.....	19
2.3.1(a) Principle.....	19
2.3.1(b) Experiment.....	20
2.3.2 Microstructure by Transmission Electron Microscopy (TEM)...	21
2.3.2(a) Principle.....	21
2.3.2(b) Experiment.....	21
2.3.3 Optical Characterization using UV-VIS Spectrophotometer.....	23
2.3.3(a) Principle.....	23
2.3.3(b) Experiment.....	24

2.3.4 Magnetic Measurements using Magnetic Property Measurement System (MPMS).....	24.
2.3.4(a) Principle.....	24
2.3.4(b) Experiment.....	26
2.3.5 Transport Measurements using Physical Property Measurement System (PPMS).....	27
2.3.5(a) Principle.....	27
2.3.5(b) Experiment.....	28
2.4 Summary.....	28
<b>3. RESULTS FOR BULK SAMPLES</b>	
3.1 Introduction.....	30
3.2 Structural Analysis.....	30
3.3 Transmission Electron Microscopy.....	33
3.4 Magnetic Characterization.....	33
3.5 Summary.....	39
<b>4. STRUCTURAL AND OPTICAL PROPERTIES OF THIN FILMS</b>	
4.1 Introduction.....	41
4.2 Structural Characterization.....	41
4.3 Optical Properties.....	43
4.4 Summary.....	50
<b>5. TRANSPORT AND MAGNETIC PROPERTIES OF THIN FILMS</b>	
5.1 Introduction.....	52
5.2 Transport Properties.....	52.
5.3 Magnetic Properties.....	56
5.4 Summary.....	62
Conclusions .....	64
References.....	66

## LIST OF FIGURES

1.2 (A) a Magnetic Semiconductor (B) a Dilute Magnetic Semiconductor (DMS) (C) a non-magnetic semiconductor.....	2
1.3 Moore's Law: Number of transistors per square inch on a single chip doubles approximately after every two years.....	5
1.4 Wurtzite Structure of ZnO.....	6
2.2.2 Experimental setup for thin film fabrication.....	18
2.3.1 Schematic diagram for a X-Ray Diffractometer.....	20
2.3.2 Schematic view of a TEM column.....	22
2.3.3 Block diagram of a UV-VIS Spectrophotometer.....	23
2.3.4 Basic principle of SQUID.....	25
2.3.5(a) Schematic diagram of Hall Effect.....	27
2.3.5(b) Four probe configuration for Hall Effect and resistivity measurements.....	28
3.2(a) XRD patterns for $x=0, 0.05, 0.10$ and $0.20$ . All ZnO peaks have been indexed.....	31
3.2(b) XRD patterns for $x=0.25$ and $0.30$ , the impurity peaks have been indexed.....	32
3.3(a)-(f) TEM micrographs and their corresponding Diffraction Patterns.....	34
3.4(a) Specific magnetization as a function of temperature for FC case.....	35
3.4(b) Specific magnetization as a function of temperature for ZFC case.....	35
3.4(c) High temperature Curie-Weiss fits for $x=0.10, 0.20$ and $0.30$ .....	37
3.4(d) Curie-Weiss Temperature, Curie constant and effective Bohr magneton number as a function of Co concentration.....	38
3.4(e) Exchange integral $J$ as a function of Co concentration.....	39
4.2(a) XRD pattern for thin films with $x=0, 0.05, 0.10, 0.20, 0.25$ and $0.30$ . All ZnO peaks, substrate peaks and 'second' phase peaks have been indexed.....	42
4.2(b) Variation of lattice constant $c$ with increase in Co concentration.....	43
4.3(a) Transmission spectra for $x=0, 0.05, 0.10$ and $0.20$ .....	45
4.3(b) Reflectance spectra for $x=0, 0.05, 0.10$ and $0.20$ .....	45
4.3(c) Splitting of 3d levels of $\text{Co}^{2+}$ in presence of tetrahedral crystal field.....	46
4.3(d) Magnified views of the absorption bands observed for $x=0.05, 0.10$ and $0.20$ .....	47
4.3(e) $\alpha^2$ as a function of energy (eV) for $x=0, 0.05, 0.10$ and $0.20$ .....	48
4.3(f) Red shift of optical band edge with increase in Co concentration.....	49
5.2(a) Variation of room-temperature resistivity with Co concentration.....	53
5.2(b) Variation of resistivity with temperature for all values of $x$ ranging from $x=0$ to $x=0.30$ .....	54
5.2(c) Variation of carrier concentration with temperature for all values of $x$ .....	55
5.2(d) Variation of Hall mobility with temperature for all values of $x$ .....	56
5.3(a) M-H curve for $x=0.20$ at 10K.....	57
5.3(b) M-H curve for $x=0.30$ at 10K.....	57



5.3(c) M-H curve for sapphire substrate at 10K.....	58
5.3(d) M-T curve for $x = 0.10$ at 200 Oe.....	59
5.3(e) M-T curve for $x = 0.20$ at 200 Oe.....	59
5.3(f) M-T curve for $x = 0.30$ at 200 Oe.....	60
5.3(g) Curie-Weiss fits at high temperature for $x = 0.10, 0.20$ and $0.30$ .....	61

# CHAPTER 1

## INTRODUCTION

---

### 1.1 BACKGROUND

The incorporation of spin functionality in a semiconductor remained an elusive dream for the entire scientific community until the discovery of a Dilute Magnetic Semiconductor (DMS) in the early eighties. The importance of such integration in a single material cannot be underestimated, as the concept alone, has opened new vistas of research called “Spintronics”[1]: a field that promises to revolutionize present day electronics.

Electronic devices till now have exploited only the charge of an electron; the spin remaining largely unexploited except for in memory device applications. As the spin can have two states, either up or down, it implies a greater degree of freedom for the electron, which in turn means the same electron, can carry additional information. This is practically possible in a “spintronic” device if there is long-range spin ordering at room temperature. It is with this picture in mind that we are looking for a material with semiconducting properties as well as room temperature (RT) ferromagnetism.

Magnetic semiconductors [2] like europium chalcogenides and semi conducting spinels had been extensively studied in the late sixties to early seventies. Though ferromagnetism and semi conducting properties co existed in these materials, advancement in their studies was stunted by the fact that they suffered from certain basic flaws like: (1) A crystal structure quite different from that of Si and GaAs which are the mainstay of electronics industry, (2) a very difficult and time consuming crystal growth, and (3) a Curie temperature significantly lower than the room temperature which limited their use to any practical purposes. There was also little hope of a dramatic improvement of the  $T_C$  of these materials.

## 1.2 MAKING OF A DMS

A semiconductor has always been known for an extrinsic doping which can enhance its properties in many ways. It was with this basic familiarity that the idea of doping a non-magnetic semiconductor with a magnetic element developed about two decades ago. The distinction between a semiconductor, a magnetic semiconductor and a dilute magnetic semiconductor is pictorially depicted below:

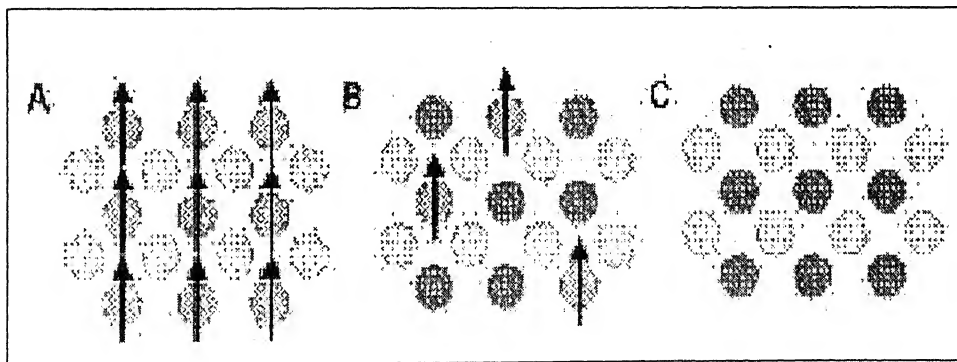


Figure 1.2 (A) a Magnetic Semiconductor (B) a Dilute Magnetic Semiconductor (DMS)  
(C) a non-magnetic semiconductor

A simple DMS can be classified as either II-VI or III-V depending upon the host semiconductor, although there are three component systems as well, such as chalcopyrites. The magnetic element used for doping has been primarily Mn for both the cases although doping with other transition elements like Co, Fe and Cr have also been studied [3]. Research in this area has been mainly concentrated on II-VI DMS such as ZnSe, CdSe, HgTe [4], [5] etc. and very recently on oxide based DMS [6], due to the ease with which magnetic ions can be introduced into their lattice to high levels of concentration. The growth of any DMS is done in the form of thin films with the deposition techniques varying from molecular beam epitaxy, sputtering, and laser ablation to sol-gel methods. It is important to mention here that the physical properties of a DMS are very sensitive to the growth methods and experimental conditions, and this is primarily the reason why there cannot be any consensus sometimes among different experimental research groups.

Though the first signs of a ferromagnetic ordering well above 100K were discovered in GaAs doped with Mn (III-V based DMS) [7], a DMS based on III-V semiconductor suffers due to a low equilibrium solubility of transition metals in the host lattice. When these compounds are synthesized under non-equilibrium conditions to enhance the solubility, the crystal structure has a large number of growth related defects, which adversely affect the electronic properties. Theoretical predictions of room temperature ferromagnetic ordering in p-type DMS by Dietl et al [8], was a silver lining and it gave a tremendous boost to the ongoing search for a semi conducting material with room temperature ferromagnetism. Similar predictions by Sato and Yoshida [9] for n-type ZnO based DMS were reported almost during the same period. It was with the reported RT ferromagnetism in Co doped anatase TiO<sub>2</sub> thin films by Matsumoto et al [10], that

attention was directed towards II-VI oxide based DMS [6]. The discovery thus gave an impetus to research being conducted on ZnO as well, with transition metal doping such as Mn and Co.

### 1.3 MOTIVATION FOR THE PRESENT WORK

Zinc oxide (ZnO) attracts attention as the host lattice for II-VI DMS for several reasons:

1. It is an intrinsically n-type [11,12] wide band gap ( $\sim 3.37$  eV) semiconductor, which is transparent in the visible regime of the electromagnetic spectrum.
2. With appropriate doping its conductivity can be enhanced, making it a very good “transparent conductor” finding applications in solar cells, flat panel displays etc.
3. It has a high exciton binding energy ( $\sim 60$  meV), which makes the electron-hole recombination process stable at room temperature [13]; useful for optoelectronic devices such as OLEDs.
4. In addition, it has been predicted to show room temperature ferromagnetism if doped with a transition metal element like Mn or Co [8]. However, this property is a hot spot currently with no conclusive results. In case, this prediction materializes without any exceptions, it could pave way for future “spintronic” devices.

The need for spintronic devices arises out of the ever-increasing demand for greater storage power in the same amount of space (limitation of space being due to the constraints of Moore’s law), faster processing, and low power consumption.

Figure 1.3 shows that Moore’s law has already started showing a deviation and the time is not far off when it would fail, as there are physical barriers to the fabrication of number of transistors on a single chip such as high leakage currents and quantum tunneling effects. The fabrication cost of putting millions of transistors together is also

enormous. Thus, we can conclude that miniaturization cannot continue forever. We have to find an alternative means to fulfill our needs as mentioned above.

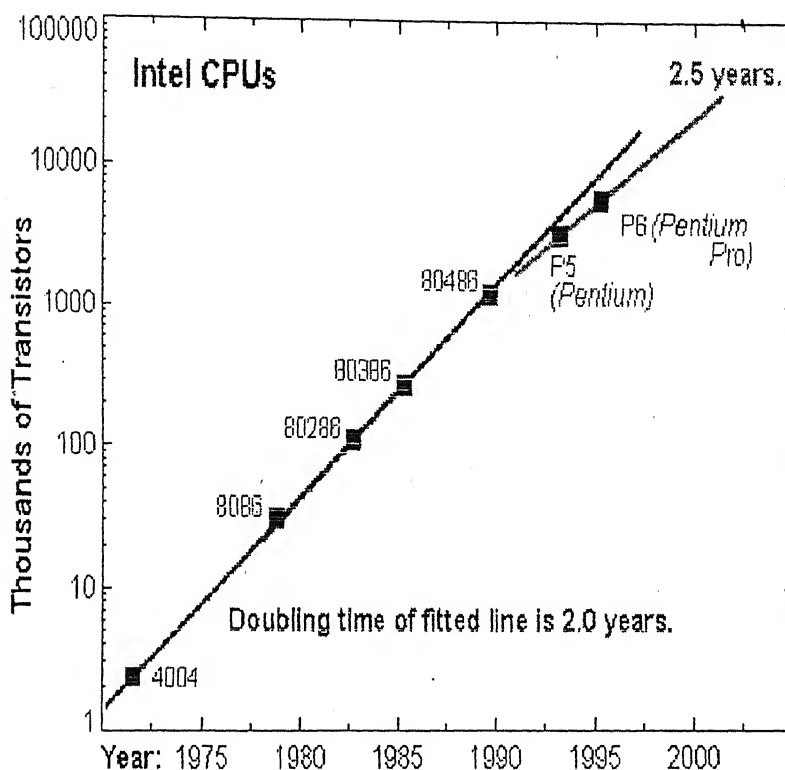


Figure 1.3 Moore's law: Number of transistors per square inch on a chip doubles approximately after every two years

## 1.4 STRUCTURAL PROPERTIES

Oxides are generally known to be insulators but ZnO seems to be an exception in the sense that it is found to be intrinsically n type due to Zn rich regions such as Zn interstitials or oxygen vacancies. It cannot be said with conviction whether the electron donors come from Zn interstitials or O-vacancies or both. ZnO crystallizes in the wurtzite form, which is shown in Figure 1.4.

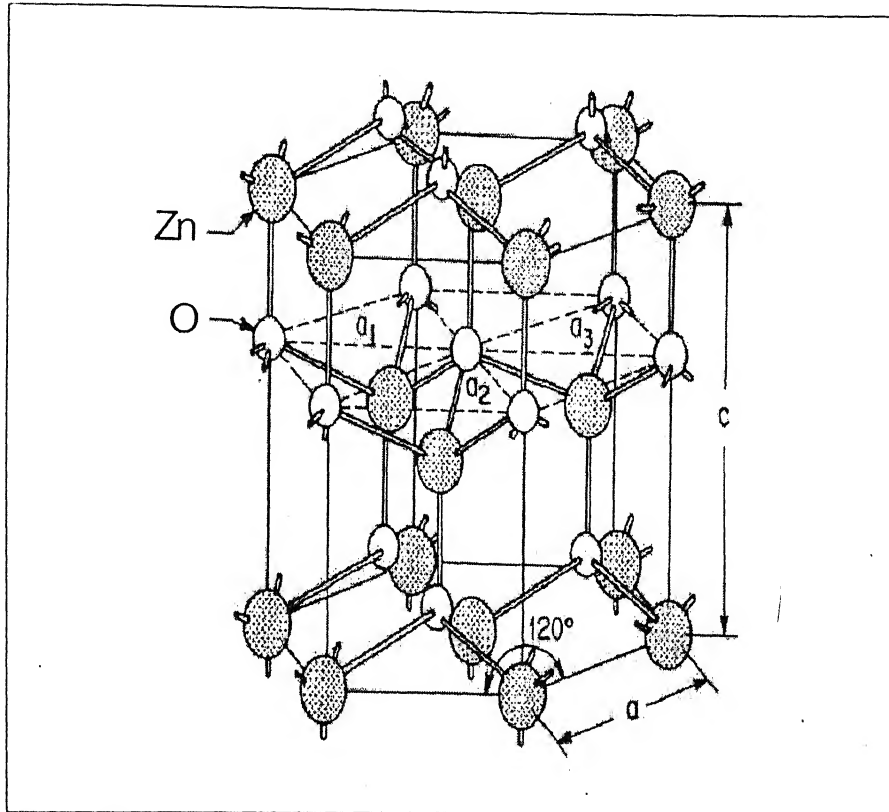


Figure 1.4 Wurtzite structure of ZnO

The zinc ions in this structure are in a tetrahedral cage of the oxygen ions. The lattice parameters of the structure are  $a = 3.249 \text{ \AA}$  and  $c = 5.205 \text{ \AA}$  [14] and the ionic radius of  $\text{Zn}^{2+}$  in tetrahedral coordination is  $0.60 \text{ \AA}$  [15], [16]. Substitution of Co at the Zn sites puts the  $\text{Co}^{2+}$  ions (ionic radius =  $0.58 \text{ \AA}$ ) in the tetrahedral crystal field of oxygen. The ground state of the  $\text{Co}^{2+}$  is the high spin state with a site spin of  $3/2$ .

For polycrystalline bulk samples, the maximum solubility limit of Co in the ZnO lattice at room temperature has been reported to be 20 percent by Kolesnik et al [17] and Risbud et al [16]. There is a large variation in the reported solubility of Co in thin films of ZnO. For example, Kim et al [18], [19] report solubility as high as 40 percent in

films deposited at 600 °C in reduced oxygen pressure of  $\sim 10^{-5}$  Torr. In general, the maximum solubility limit and hence the homogeneity of thin films has been found to depend on growth conditions such as substrate temperature, oxygen pressure [18] and the technique of deposition. The variation of the lattice constant on substitution of Co in ZnO both by sol-gel method [20] and Pulsed Laser Deposition (PLD) [21] and that of Mn in ZnO by PLD [22] has been found to follow the Vegard's law till the maximum solubility limit is achieved.

## 1.5 ELECTRON MICROSCOPY

Transmission Electron Microscopy (TEM) is a commonly used technique to establish solubility limits and to identify the presence of impurity phases. Risbud et al [16] have used TEM measurements on bulk polycrystalline samples of  $\text{Zn}_x\text{Co}_{1-x}\text{O}$  with  $x = 0.15$  and  $x = 0.25$ . Their TEM images suggest single crystals of varying sizes with larger size corresponding to the higher Co composition. The defect formation and inhomogenous contrast in the single crystals, which they have observed, could be possibly due to the precipitation of the "second" phase in the samples. However, they have found no direct evidence of Co clustering even for  $x = 0.25$  where a second "spinel" phase had been detected by XRD.

TEM studies done by Shinde et al [23] present clear evidence of Co metal clustering from electron diffraction pattern in highly reduced Co-doped rutile  $\text{TiO}_2$  thin films deposited by PLD. These clusters are present at the film-substrate interface, their size being 9-10nm in diameter. STEM studies done again by Shinde et al [24], on Co (7 at%) doped anatase  $\text{TiO}_2$  thin film samples deposited by PLD, has confirmed the presence of Co clustering in the films and also the incorporation of a small fraction of Co in the remaining  $\text{TiO}_2$  matrix.



On the other hand, STEM studies done by Ogale et al [25] on Co doped rutile  $\text{SnO}_2$  thin films deposited by PLD, with  $x$  as high as 0.27, have not shown any detectable Co clustering in their samples and the microstructure of the films remains uniform.

## 1.6 OPTICAL PROPERTIES

Zinc oxide has a direct band gap of  $\sim 3.37$  eV. Optical spectra of transition metal substituted ZnO are likely to show features related to d-d transitions between the energy levels of the transition metal.

Roth et al [26] have studied heavily defect doped thin films of ZnO deposited by various techniques. The electron density in their samples varied from  $5 \times 10^{17}$  to  $2 \times 10^{20} / \text{cm}^3$ . They observed band gap shrinkage above a critical concentration known as Mott critical density. This shrinkage competes with band gap widening called Burstein-Moss effect. Both these mechanisms are found to be dependent on the electron density.

Optical characterization has been done for conducting films of ZnO [27], [28], [29] and for those doped with Co, by certain groups [30], [31]. The n-type ZnO films are found to be highly transparent in the visible regime with certain absorption bands appearing around  $\sim 2$  eV for films with additional Co doping. These bands have been attributed to the d-d transition of  $\text{Co}^{2+}$  ions. Kim et al [30] have observed a red shift of the absorption edge with increasing Co concentration in films deposited by rf magnetron sputtering. The transmission spectra and variation of band gap in ZnO films doped with Mn and deposited by PLD has been recorded by Fukumura et al [22]. They have found a blue shift in the band gap with increase in Mn concentration.

Simpson et al [32] too have observed a blue shift of the optical band edge with increase in Co concentration in Co doped anatase  $\text{TiO}_2$  films grown by PLD.

## 1.7 TRANSPORT PROPERTIES

The conductivity of ZnO films can be further increased by doping them with n type impurities such as Al, In and Sn. The doped films can be made highly degenerate with carrier concentration as high as  $\sim 10^{21}/\text{cm}^3$ . A p-type doping of ZnO has been practically difficult to achieve. However, recent efforts to dope these films with p type impurities such as Phosphorous [33] and Nitrogen [34] have seen some success. The resistivity of the n-type doped films with Co substitution has been found to show predominantly a metallic character [21]. The typical values of resistivity are  $\sim 10\text{m-ohm cm}$ . A systematic study of the temperature dependence of resistivity in films with varied Co concentration is, however, lacking. Hall mobility of Co doped ZnO thin films grown by PLD as measured by Kim et al [19] is found to decrease with an increase in the Co concentration. It shows a sudden fall at the onset of phase segregation i.e. when the doping level reaches the maximum solubility limit of 40 percent. Marcel et al [35] have studied the temperature as well as doping dependence of Hall mobility in In doped ZnO thin films. The Hall mobility was found to decrease with respect to either of the two parameters. They have attributed these results mainly to electron scattering by oxygen vacancies that act as ionized impurities at low temperature and optical phonons at high temperatures.

## 1.8 MAGNETIC PROPERTIES

A ferromagnetic substance would show spontaneous magnetization below the Curie temperature  $T_c$ . This can be established through measurements of field cooled (FC) and zero field cooled (ZFC) magnetization. In the presence of sufficient domain boundary pinning, one expects the FC and ZFC branches of magnetization to bifurcate below a critical temperature. A substance with ferromagnetic ordering would also show a highly

non-linear dependence of magnetization on the applied magnetic field. The M-H curves are often hysteretic. At  $T \gg T_c$ , the magnetic susceptibility of the ferromagnetic material follows the Curie – Weiss law:

$$\chi = C_o / (T - T_o)$$

where  $\chi$  is the susceptibility in units of emu/g Oe,  $C_o$  = Curie constant and  $T_o$  = Curie-Weiss temperature. The Curie constant  $C_o$  is defined as:

$$C_o = N g_{\text{eff}}^2 \mu_B^2 S(S+1) / 3 k_B$$

where  $N$  is the number of Co atoms per gram,  $g_{\text{eff}}$  is the effective gyromagnetic factor,  $\mu_B$  is the Bohr magneton,  $S$  is the spin of the  $\text{Co}^{2+}$  and  $k_B$  is the Boltzmann constant. The effective number of Bohr magnetons is further defined as:

$$\mu_{\text{eff}} = g_{\text{eff}} [S(S+1)]^{1/2}$$

assuming complete quenching of the orbital magnetic moment.

The Curie constant is also related to the exchange integral  $J$  between nearest neighbor as well as second and higher order  $\text{Co}^{2+}$  neighbors in the following manner:

$$J = 3k_B T_o / S(S+1)$$

Thus from the straight line fit of the Curie Weiss law at high temperatures, we can evaluate macroscopic variables like  $T_o$  and  $C_o$  which in turn help us in evaluating important microscopic variable such as  $\mu_{\text{eff}}$ ,  $g_{\text{eff}}$  and  $J$  for the system.

The M-H and M-T measurements also provide valuable information about formation of ferromagnetic clusters, superparamagnetism and spin glass behavior.

The magnetic state of ZnO doped with Co remains controversial with certain groups claiming the predicted room temperature ferromagnetism [18], [21] while others declaring results contrary to the predictions [3], [17]. These experiments have been

performed mainly on thin films grown by PLD. Recent papers emphasize the fact that observation of room temperature ferromagnetism in Co doped ZnO is subjected to the additional condition of hole doping [16], [36], which is practically difficult to achieve in ZnO. A latest theoretical study [37] observes that the ferromagnetic coupling has a very short-range nature. A high concentration of Co with sufficient electron carriers is required to induce any ferromagnetic interactions within this short-range ( $\sim 4\text{\AA}$ ). It is important to mention here that Co has been observed to suppress electron carrier concentration [19]. Thus it requires an optimization between the two conditions and when it is not met, the AFM coupling dominates over the FM coupling as the two are always in competition.

## 1.9 HIGHLIGHTS OF THE PRESENT THESIS

Having introduced the subject of DMS and the importance of the present work in this chapter, we shall discuss the various characterization techniques for our II-VI DMS, which are in the form of n-type Co doped ZnO thin films synthesized with Pulsed Laser Ablation, in the subsequent chapters.

Chapter 2 describes the preparation method of targets and thin film fabrication by Pulsed Laser Ablation. Some basic principles of characterization techniques that have been used are also described in Chapter 2.

Chapter 3 deals with the structural, electron microscopy and magnetic properties of the samples in bulk; the characterization techniques for them being XRD, TEM and SQUID respectively.

Chapter 4 shall describe the structural and optical characterization of thin film samples done with XRD and UV-VIS spectrophotometer.

Finally, in Chapter 5 we discuss the transport and magnetic properties studied over a wide range of temperature and magnetic field strength.

A summary has been provided at the end of each chapter.

## CHAPTER 2

# THIN FILM FABRICATION & CHARACTERIZATION TECHNIQUES

---

### 2.1 INTRODUCTION

In this chapter, we describe experimental methods used to synthesize thin films and bulk samples of electron doped  $\text{Zn}_{1-x}\text{Co}_x\text{O}$ , and a variety of techniques used to characterize crystal structure, optical transmission, magnetic properties and electrical transport.

#### PART A:

### 2.2 PREPARATION OF THIN FILMS AND BULK SAMPLES

There are a number of ways, ranging from molecular beam epitaxy (MBE), laser ablation, sputtering, sol-gel methods etc. by which thin films of Dilute Magnetic Semiconductors (DMS) can be synthesized. Out of these, laser ablation has been found to be quite successful in growing high quality epitaxial thin films of a number of DMS compounds. While growing a thin film, we are primarily concerned that it should show properties similar to a bulk single crystal. In the first part of this section, we shall

discuss target preparation and thin film fabrication with small inputs on the principle of an excimer laser and on the design of the deposition chamber. In the latter part of the chapter, we shall describe the principles of characterization techniques that we have used and the experimental details of every measurement that has been done.

### 2.2.1 TARGET PREPARATION

The required oxides were taken in stoichiometric proportions in powder form and ground thoroughly for one hour to ensure mixing at the cationic level. The oxides, their source and purity percentage are given below:

ZnO	Aldrich Chemicals, USA	99.99%
Al <sub>2</sub> O <sub>3</sub>	Strem Chemicals, USA	(99.999%-Al)
Co <sub>3</sub> O <sub>4</sub>	Strem Chemicals, USA	99.5%

The powder was annealed at 1150°C for 12 hrs. The grinding and annealing process was repeated three times to ensure homogeneous mixing. The annealed mixture was pelletized using a 2 cm diameter die. The pelletization was done under 40 KPa pressure using a hydraulic press. Final sintering was done at 1300 °C to make the targets very dense and hard for ablation purposes. Sintering is done at such high temperatures (usually about  $\frac{3}{4}$  times the melting point of the sample, which is primarily ZnO here (MP = 1975 °C) in order to reduce porosity and hence cause a densification of the pelletized samples. All sintered pellets were green in color, the intensity of green being proportional to the Co content except for the sample without cobalt, which was cream in color.

### 2.2.2 THIN FILM FABRICATION

#### 2.2.2(a) TECHNIQUE OF PULSED LASER ABLATION

Film growth via pulsed laser ablation can be carried out in a reactive environment containing any kind of gas. As the laser beam impinges on the target, photons are absorbed by the surface, forming a surface molten layer. This layer is referred to as a "Knudsen Layer". The vaporization process, which takes place in a very short time but with a considerable amount of mass transport, exerts a strong recoil pressure on the liquid layer and expels the molten droplets. The droplets then form a plume consisting of a mixture of energetic species including atoms, molecules, electrons, ions, clusters, micron sized particulates and molten globules. The collisional mean free path inside the dense plume is very short. As a result, immediately after laser irradiation, the plume rapidly expands into the vacuum from the target surface to form a nozzle jet, which then strikes the substrate on which the film is to be deposited.

Pulsed Laser Deposition (PLD) offers many advantages over other techniques of film growth, these include:

1. It can be used to vaporize and to deposit thin films of any material if the absorbed laser power density is high enough.
2. The use of short laser pulses offers the advantage of congruent evaporation. Congruent evaporation in turn allows PLD to preserve the stoichiometry during mass transfer from target to thin film.
3. A PLD system can produce films with quality comparable to MBE systems that cost ten times as much and more.



4. The laser is independent of the deposition system. Thus complex multilayer thin films are straightforward to produce within a single system by moving various targets into and out of the beam focal point.
5. Very precise control over growth rate can be achieved by tuning the pulsed energy and repetition rate.

However, there are certain disadvantages too:

1. Formation of a liquid layer due to laser irradiation can cause “splashing” of micron sized particles and sometimes deviation from congruent evaporation.
2. Formation of crystallographic defects due to bombardment of the growing film by highly energetic particles from the plume.

#### **2.2.2(b) EXCIMER LASER**

The useful range of laser wavelengths for thin film growth by PLD lies between 200 nm and 400 nm as most materials used for deposition work exhibit strong absorption in this spectral range. The excimer is a gas laser, which emits its radiation directly in the UV region and hence is the choice for most PLD work.

We have used a commercial excimer laser Lumonics 'PM – 800. The gases used are supplied from separate high pressure cylinders. The laser is operated at 4700 mbar. The system can achieve pulse repetition rates up to 20 Hz with energies  $\sim 650$  mJ/pulse. The filling of gas for laser operation, control of the number of laser pulses, pulse repetition rate and pulse energy are all done by the laser's microprocessor control.

#### **Principle of Excimer Laser**

An excimer is a diatomic molecule, which forms and exists only in an excited state. The excimer molecules are formed in a gaseous mixture of their component gases like in case of KrF laser. Energy is pumped into the gas mixture through avalanche

electric discharge excitation. The pumping creates ionic and electronically excited species that react chemically and produce the excimer molecules. Once the excimer is formed, it will decay via spontaneous emission and collisional deactivation. The lasing action takes place between a bound upper electronic state and a repulsive or weakly bound ground electronic state. The ratio of upper state lifetime to lower state lifetime is high and therefore, population inversion and hence high gain are easily achieved.

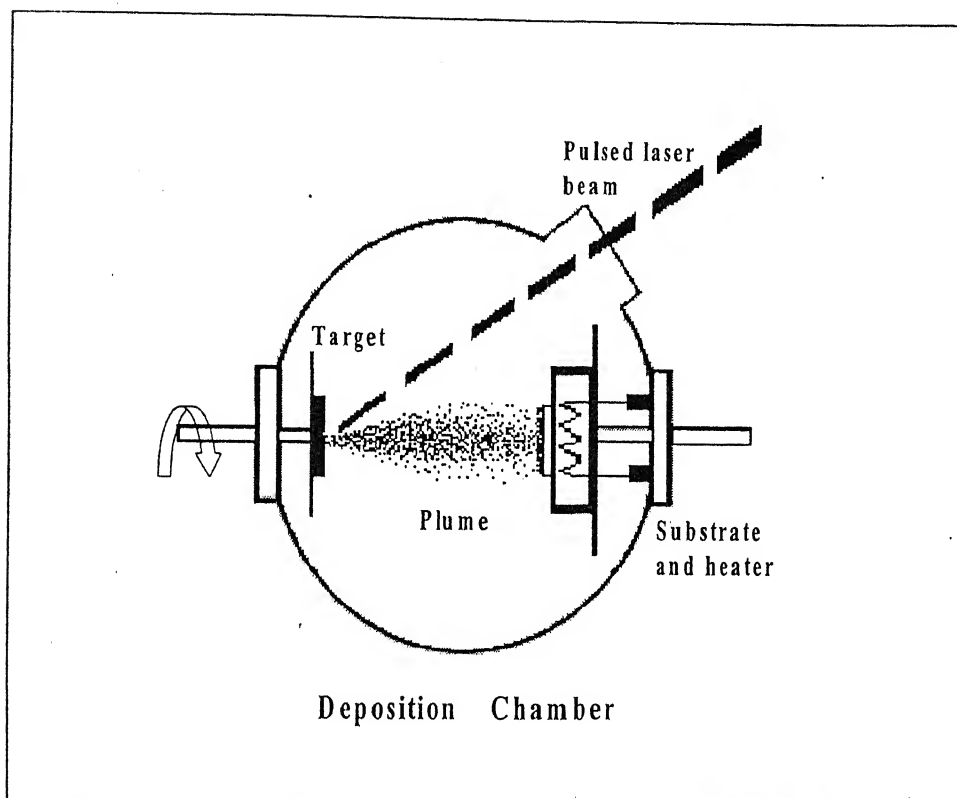
### 2.2.2(c) VACUUM CHAMBER

The stainless steel chamber is evacuated by a combination of a rotary and an oil diffusion pump to a base pressure of  $\sim 10^{-6}$  Torr. The oil vapors generated by the heating of the diffusion pump oil have a finite probability to reach the chamber. To prevent this, the chamber has been provided with a liquid nitrogen trap. The chamber is equipped with a multi-target carousel and a substrate heater capable of reaching  $\sim 800^{\circ}\text{C}$  in oxygen environment. The chamber also has provision for inletting desired gases through a mass flow controller and a quartz window for entry of laser beam.

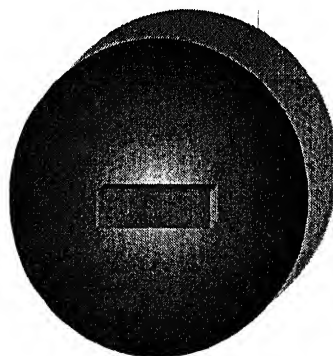
### 2.2.2(d) EXPERIMENTAL SETUP AND DEPOSITION CONDITIONS

The experimental setup consists of a target holder and a substrate holder inside the deposition chamber. Bulk ceramic targets were glued on Aluminium holders with silver epoxy and these were mounted on the rotatable target holder. A high power excimer laser was used as an external energy source to ablate the target material. A set of optical components was used to focus the laser beam over the target surface. A schematic diagram for the arrangement is shown in Figure 2.2.2. A dummy run was taken on glass substrate for a given number of shots and film thickness was measured with a stylus profilometer (Model: ALPHA-STEP 100). In this way, the number of laser shots

required for a particular film thickness was decided. This is known as thickness calibration.



Bulk Target



Substrate Piece mounted on heater block

Figure 2.2.2 Schematic diagram for the experimental set-up

The deposition conditions for the films are summarized below:

Substrate used	Sapphire (0001)
Laser Wavelength	248 nm
Temperature of substrate	600 °C
Vacuum Pressure	$\sim 10^{-6}$ Torr
Target substrate distance	5 cm
Energy of the laser beam	200 mJ./pulse
Repetition Rate	5 Hz
Pulse Duration	20 ns

## **PART B:**

### **2.3 MEASUREMENTS OF STRUCTURE AND PROPERTIES**

#### **2.3.1 X RAY DIFFRACTION USING A DIFFRACTOMETER**

##### **2.3.1(a) PRINCIPLE**

In an X-Ray Diffraction (XRD) experiment, a collimated and monochromatic beam of X-rays is incident on the sample. Diffraction occurs in accordance with Bragg's Law:

$$2d\sin\theta = n\lambda,$$

where  $d$  is the interplanar spacing,  $\lambda$  is the incident wavelength,  $n$  the order of diffraction and  $2\theta$  the angle of diffraction. The intensity of the diffracted beam as number of counts per second is measured as a function of the diffraction angle  $2\theta$ . The diffraction pattern so obtained is used to identify the crystalline phases present in the sample.

**2.3.1(b) EXPERIMENT**

A  $\theta$ - $\omega$  diffractometer (Rich. Seifert Model No. XRD 3000P), which uses a Cu-K $\alpha$  source, was used for doing thin film measurements. A sketch of the diffraction geometry is shown in Figure 2.3.1.

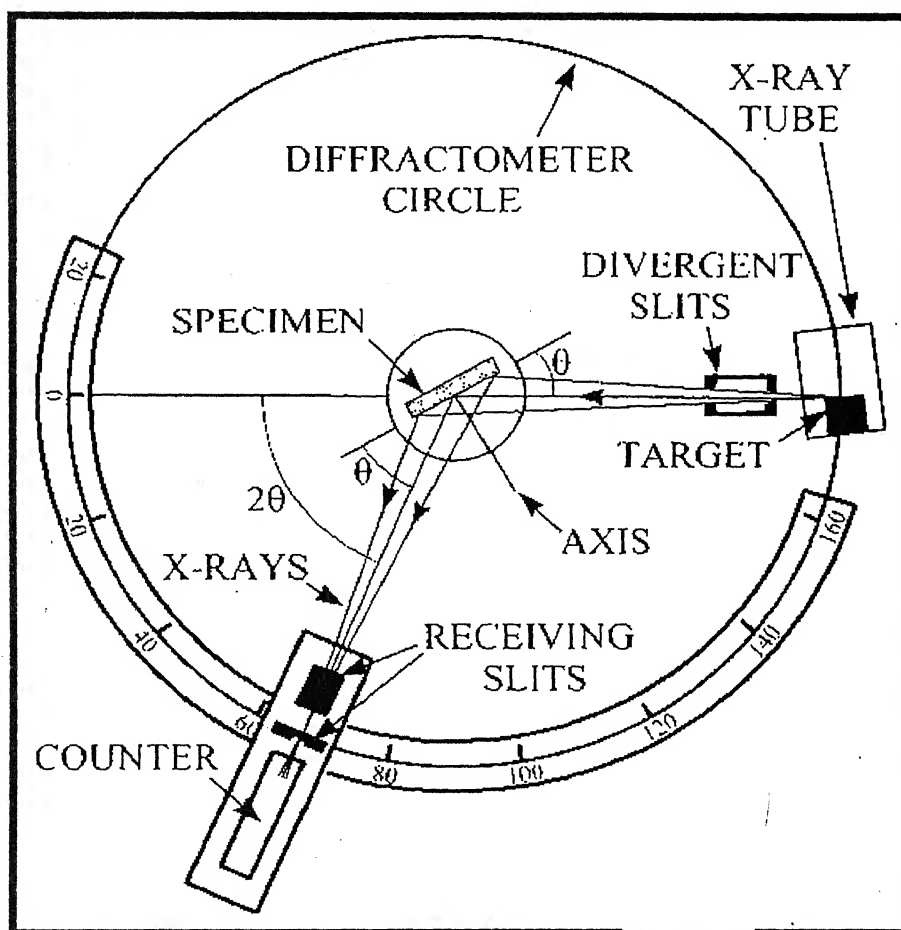


Figure 2.3.1 Schematic diagram for X-ray Diffraction

The X-Ray tube was operated at 30 kV and 20 mA. The scanning rate was 3°/min and the scanning range was from 30° to 95°. The substrate of the film acted as the “standard” in order to make corrections and evaluate lattice constant  $c$ . The data thus obtained was recorded on a computer.

### **2.3.2 MICORSTRUCTURE BY TRANSMISSION ELECTRON MICROSCOPY (TEM)**

TEM is an analytical tool that allows detailed examination of the microstructure through high-resolution and high-magnification imaging. Selected area diffraction patterns are possible, which can help in identifying the crystal structures and the phases present. The only disadvantage of TEM is that it is a destructive technique.

#### **2.3.2(a) PRINCIPLE**

The source radiation is generated with an electron gun. The electron beam passes through a series of lens and aperture system, which focuses and controls the electron beam and removes any stray electrons. The corrected beam is then incident on the sample. Image data is then collected on a fluorescent screen, which is hit by the electron beam. The resulting image can thus be recorded on a photographic film. A schmematic diagram of the TEM column is shown in Figure 2.3.2. The vacuum is generally  $10^{-6}$  Torr inside the chamber and  $10^{-7}$  Torr inside the electron gun.

#### **2.3.2(b) EXPERIMENT**

We have used a Transmission Electron Microscope (Model: JEOL (JEM 2000FX)) TEM was done on bulk samples for three different concentrations,  $x = 0, 0.20$  and  $0.30$ .

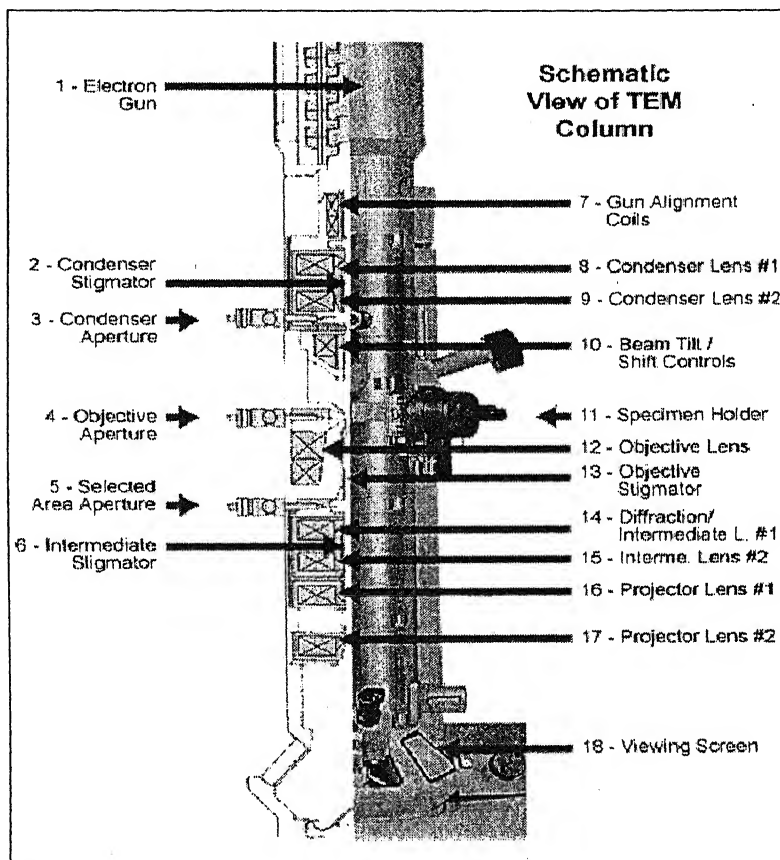


Figure 2.3.2 Schematic view of a TEM Column

A very fine powder of the samples was prepared for TEM measurements. A support film was prepared on a glass substrate using "Formvar" solution, which was allowed to float on water surface. This was transferred on the mat side of the copper specimen grid. The fine powder of the sample was then dispersed in distill water by shaking well and allowed to settle for sometime. A few drops of the suspension were then placed on the coated grid with the help of a micropipette. On drying up, the samples were examined under the Transmission Electron Microscope. The microscope was operated at 120 kV and the micrographs and Selected Area Diffraction (SAD) patterns were recorded on a 35mm photographic film.

### 2.3.3 OPTICAL CHARACTERIZATION USING UV-VIS

#### SPECTROPHOTOMETER

##### 2.3.3(a) PRINCIPLE

A Hitachi Model 150-20 UV-VIS Double Beam Spectrophotometer (190-900nm) was used for the measurements whose block diagram is shown in Figure 2.3.3.

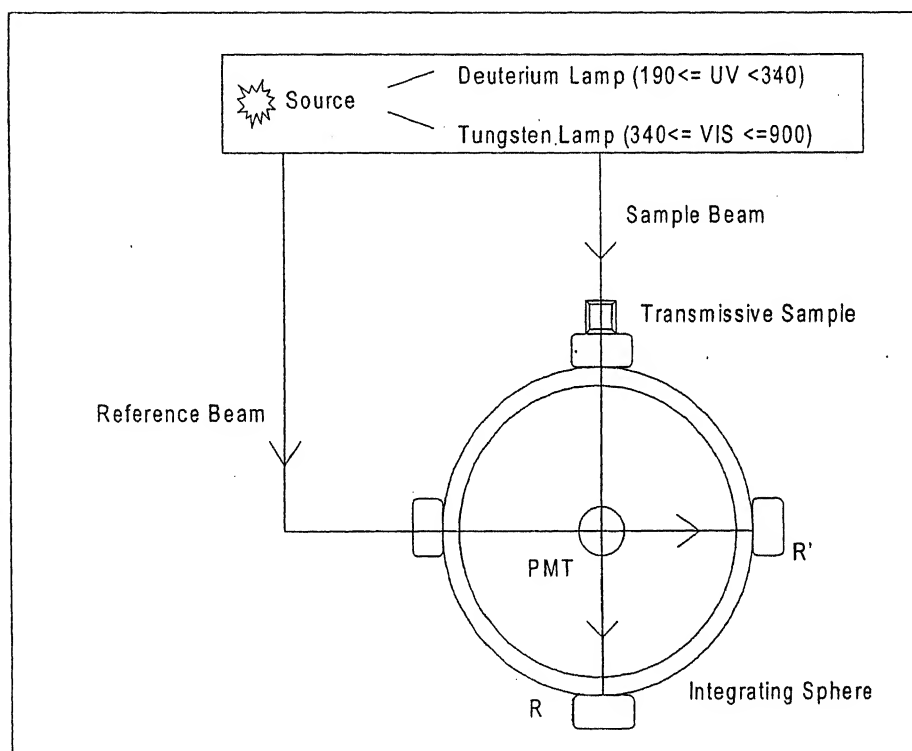


Figure 2.3.3 Block Diagram of UV-VIS Spectrophotometer

The ratio of transmitted intensity ( $I$ ) to the incident ( $I_0$ ) when light passes through an absorbing media (say, a thin film) is given by the Beer Lambert's Law:

$$I = I_0 \exp(-\alpha t) \dots\dots\dots (?)$$



where  $\alpha$  is the absorption coefficient and  $t$ , the thickness of the film. The ratio  $I/I_0$  is called the transmittance  $T$ . If reflection from the surface of the film is also considered then the transmittance  $T$  is given by,

$$T = (1-R) \exp(-\alpha t)$$

For a known  $t$ ,  $\alpha$  can be calculated from the transmission and reflection measurements.  $\alpha^2$  is thus plotted as a function of energy (eV) and a tangent is drawn at the point where absorption suddenly peaks up. The point at which this tangent cuts the x-axis gives the direct band gap in eV.

### 2.3.3(b) EXPERIMENT

For transmission measurements, the thin film samples were placed at the place shown in the block diagram. The reference for these films was a bare substrate (Sapphire) of the same size on which the films were deposited. For reflection measurements, the sample was kept at position R and reference was provided by position R', again shown in the block diagram.

### 2.3.4 MAGNETIC MEASUREMENTS USING MAGNETIC PROPERTY MEASUREMENT SYSTEM (MPMS)

#### 2.3.4(a) PRINCIPLE

The MPMS comprises of two main sections:

1. The dewar, probe and SQUID sensor which is a thin superconducting film.
2. A superconducting electromagnet, giving a field of up to 5 tesla.

Samples are mounted within a plastic straw and connected to one end of a sample rod, which is inserted into the dewar/probe. The basic principle involved is depicted in Figure 2.3.4.

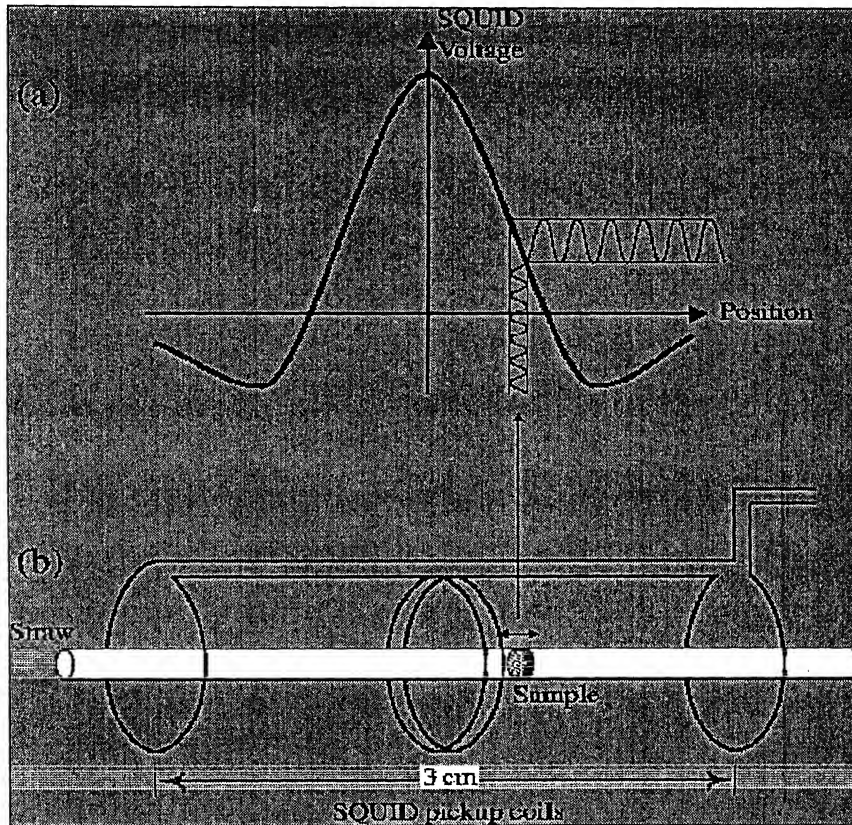


Figure 2.3.4 Basic Principle of SQUID

The other end is attached to a stepper motor, which is used to position the sample within the center of the SQUID detection coils. The detection coils, connecting wires and the SQUID input coil form a closed superconducting loop. As the sample is made to oscillate within the detection coils by the motor, the change in its position induces a flux within the detection coils thereby inducing a current in the superconducting circuit. This current is converted into a voltage signal by the SQUID, which is an ideal current-to-voltage converter. This voltage is a periodic function of the applied magnetic flux. In this way, we can detect very small magnetic fields by monitoring the voltage changes.

### 2.3.4(b) EXPERIMENT

We have used a Quantum Design MPMS for magnetic measurements.

The bulk and thin film samples used for these measurements had  $x = 0.10, 0.20$  and  $0.30$ . For measurements on bulk samples, about  $\sim 5\text{mg}$  of the powder was placed in a plastic capsule, which was mounted at the center of the standard plastic straw sample holder of the MPMS system. Magnetization of the films was measured by aligning the external magnetic field parallel to the plane of the film. In both the cases the background signal of a bare substrate and of the capsule and straw were taken for accurate determination of the magnetic moment of the samples. The data for the magnetization curves (M-T) was obtained at a field of 500 Oe for two cases: (i) by warming after having cooled under zero-field-cooled (ZFC) condition, and (ii), by warming after having cooled under an applied field (FC). The temperature range for the measurements was 350 K down to 10 K with a step size of 5 K. M-H measurements were done for thin films at a temperature of 10 K and the scanning range was from +500 Oe to -500 Oe with a step size of 20 Oe. M-T measurements were done for both ZFC and FC condition at a field of 200 Oe with a step size of 10 K and the temperature range being 10 K – 350 K. The background correction was done for the substrate by running a bare substrate of the same size and subtracting its contribution from that of the film-substrate system.

### **2.3.5 TRANSPORT MEASUREMENTS USING PHYSICAL PROPERTY MEASUREMENT SYSTEM (PPMS)**

#### **2.3.5(a) PRINCIPLE**

##### **Hall Effect and Resistivity Measurement**

The sample is placed in a magnetic field perpendicular (z direction) to the plane of the sample. When an electric field is applied across the sample, a current flows in the x direction. The majority charge carriers (electrons in this case), drift in the y direction

under the influence of the magnetic field (Lorentz force). As electrons begin to accumulate on one side of the sample, a transverse electric field is established on the opposite face which just cancels the effect of the Lorentz force due to the magnetic field. This is known as the Hall field.

The quantity defined by  $R_H = E_y / j_x * B = -1/n * e$  is called the Hall coefficient. Its sign is determined by the sign of the majority charge carriers. The important parameters which can be determined from the Hall Effect are the majority carrier concentration, their sign and the Hall mobility. A schematic diagram for Hall Effect is shown in Figure 2.3.5(a). The four-probe method is the standard way to separate out sample resistance from the “contact” resistance, its schematic view is shown in Figure 2.3.5(b). By separating out the current contacts from the voltage contacts, we are able to distinguish the sample resistance from that of contacts and connecting wires. To obtain the Hall voltage two additional contacts perpendicular to those shown were made.

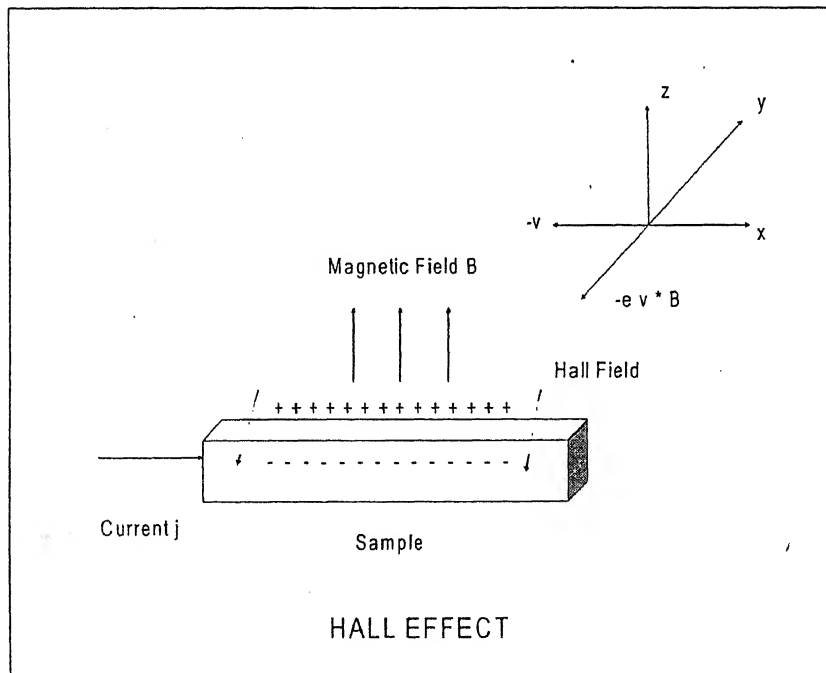


Figure 2.3.5(a) Schematic Diagram of Hall Effect

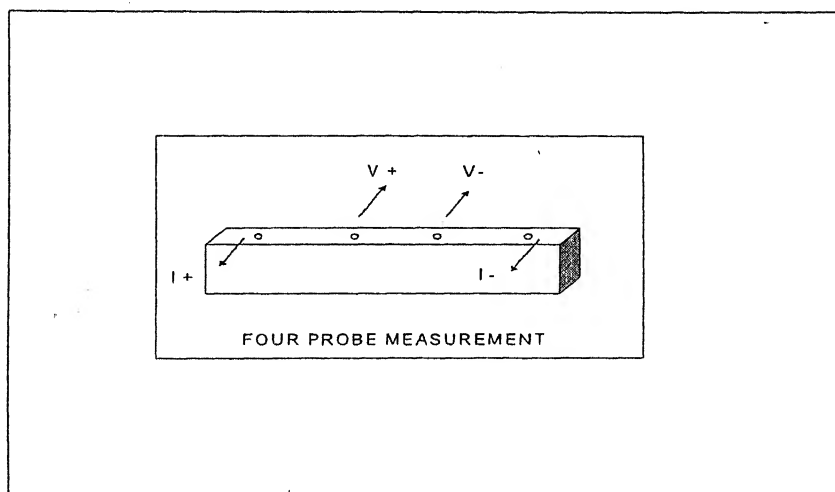


Figure 2.3.5(b) Schematic Diagram for Four Probe Measurement of resistivity

### 2.3.5(b) EXPERIMENT

The measurements were done for  $x = 0, 0.05, 0.10, 0.20$  and  $0.30$  using a Quantum Design Physical Property Measurement System (PPMS).

Gold contacts were made on thin film samples, which were placed on the puck of PPMS probe and inserted inside the dewar. The resistivity was measured at zero field. The temperature range was 315 K down to 2 K. Hall measurements were done for seven different temperatures: 10K, 20K, 30K, 50K, 100K, 150K and 200K with the field being scanned from 0 tesla to 10 tesla for each case.

## 2.4 SUMMARY

We have discussed in detail the experimental procedure for making ablation targets by the solid-state technique and thin film fabrication using Pulsed Laser Ablation. The deposition conditions during growth of films have been summarized.

We have also discussed the basic principles of the characterization techniques using schematic diagrams, wherever possible, with the details of each experiment that has been performed.

## CHAPTER 3

### RESULTS FOR BULK SAMPLES

---

#### 3.1 INTRODUCTION

In this chapter, we shall undertake a systematic study of the solubility of Co in the bulk samples of electron doped ZnO, and the effects of varying concentration of Co on the magnetic behavior of these doped samples. Although bulk, undoped samples of Co substituted ZnO have been studied earlier, the distinguishing feature of this study is the effect of electron doping on the magnetic order. We shall report studies of crystallographic structure, phase purity and magnetic behavior of bulk samples with the following compositions:

$$(\text{Zn}_{1-x}\text{Co}_x\text{O})_{99}(\text{Al}_2\text{O}_3)_1 \text{ with } x = 0, 0.05, 0.10, 0.20, 0.25 \text{ and } 0.30$$

#### 3.2 STRUCTURAL ANALYSIS

The X-ray  $\theta - 2\theta$  diffraction patterns of the powdered samples are shown in Figure 3.2 (a) and (b). As evident in the figure, all Bragg peaks in the X-ray profiles of the samples with  $x = 0, 0.05, 0.10$  and  $0.20$  can be identified with the wurtzite structure of ZnO. It is clear that within the resolution limit of X-ray diffraction ( $\sim 1$  percent phase concentration), there is no crystalline impurity phases present in these samples. These results suggest that all the Co atoms go to the tetrahedrally coordinated metal ions sites

of the wurtzite structure. Since the sintering has been carried out at high temperatures, here we do not expect any cobalt rich amorphous phases segregating at the grain boundaries.

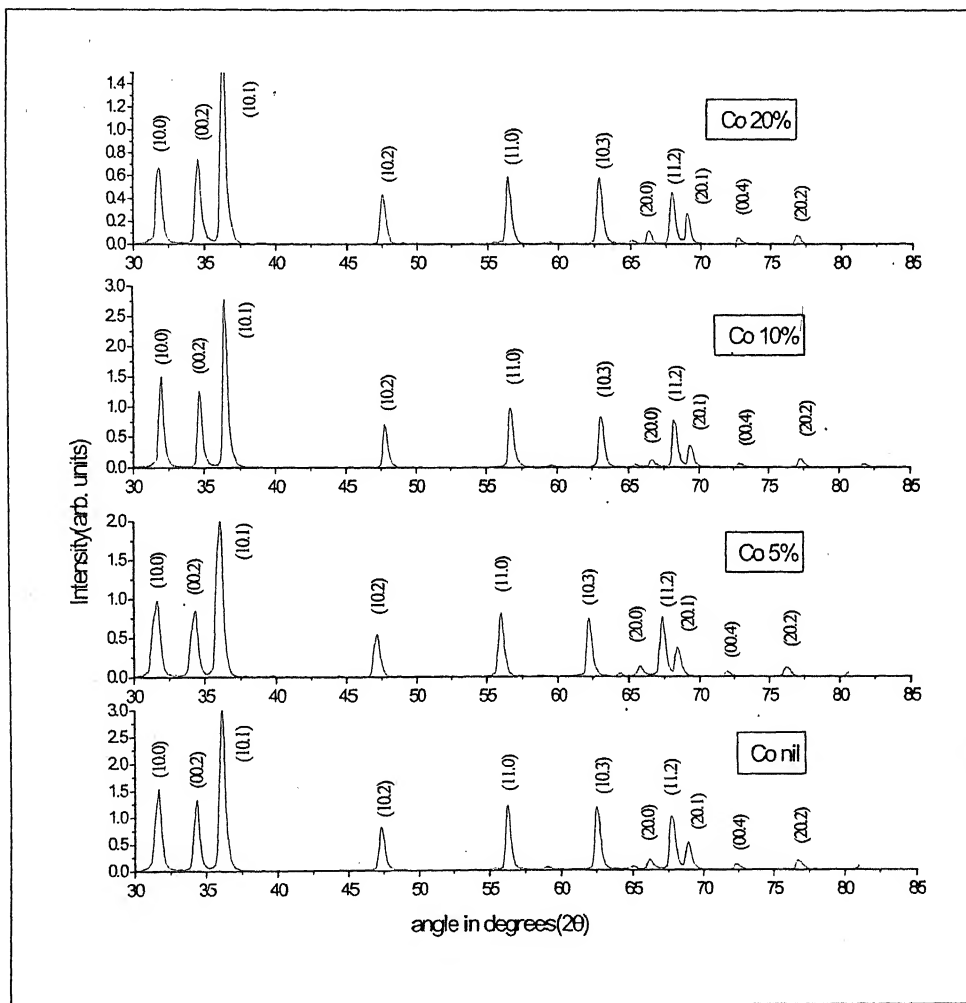


Figure 3.1(a) XRD patterns for  $x=0, 0.05, 0.10$  and  $0.20$ . All ZnO peaks have been indexed

When the Co concentration is increased to 25 percent, the formation of a two-phase mixture is evident as shown in Figure 3.2(b).



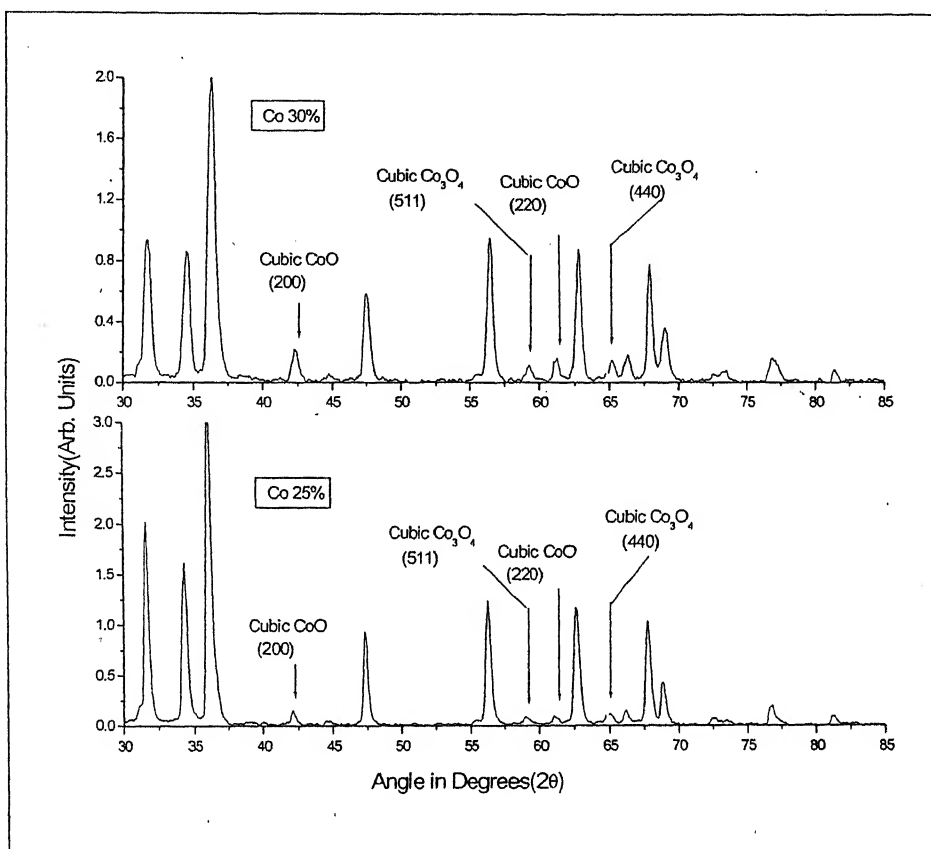


Figure 3.2(b) XRD patterns for  $x=0.25$  and  $0.30$ , the impurity peaks have been indexed

Out of the four “second phase” peaks in Figure 3.2(b), two can be identified with the cubic phase of CoO while the other two correspond to those of cubic (or spinel)  $\text{Co}_3\text{O}_4$ . The intensity of these peaks grows with the cobalt content as is reflected in the scan for  $x = 0.30$ . Thus the maximum solubility of cobalt in our electron doped ZnO samples prepared at  $1300^\circ\text{C}$  at room temperature is found to be 20 percent. Since the ionic radii of  $\text{Zn}^{2+}$  and  $\text{Co}^{2+}$  are  $0.60 \text{ \AA}$  and  $0.58 \text{ \AA}$  respectively, one does not expect a large variation in the lattice parameters of ZnO on substitution of cobalt.

### 3.3 TRANSMISSION ELECTRON MICROSCOPY

Figure 3.3(a) to 3.3(f) show transmission electron micrographs and corresponding selected area diffraction patterns of single crystal of the samples with  $x = 0$ ,  $x = 0.20$  and  $x = 0.30$ . The contrast in the microstructures reveals band like features, which are most significantly visible in Co – 20% sample. These bands are bending/extinction contours formed due to gradual thickness variation of the grain. Between the bending contours, some domain formation can be seen. The formation of these domains is presumably due to the stress induced during grounding or an inhomogeneity in the oxygen concentration. Examination of several areas in the  $x = 0.3$  samples in the microscope did not reveal the presence of the CoO precipitates. Since precipitation is present, as clearly seen in X-ray profiles [Fig.3.1 (b)], there was every possibility of finding the precipitate as such in the microscopy. But as we can study only selected areas of the sample in a TEM measurement, it is likely that the cobalt rich phase was missed in TEM scans. The diffraction patterns from the single crystals in different orientations have been recorded and they all correspond to the hexagonal phase of zinc oxide.

### 3.4 MAGNETIC CHARACTERIZATION

The zero-field-cooled (ZFC) and field-cooled (FC) magnetization (M-T) measurements were performed on three samples representing critical Co concentration. These are; (i)  $x = 0.10$ , where cobalt atoms replace Zn sites in the lattice, (ii)  $x = 0.30$ , where there is a clear evidence for phase separation and, (iii)  $x = 0.20$ , which lies

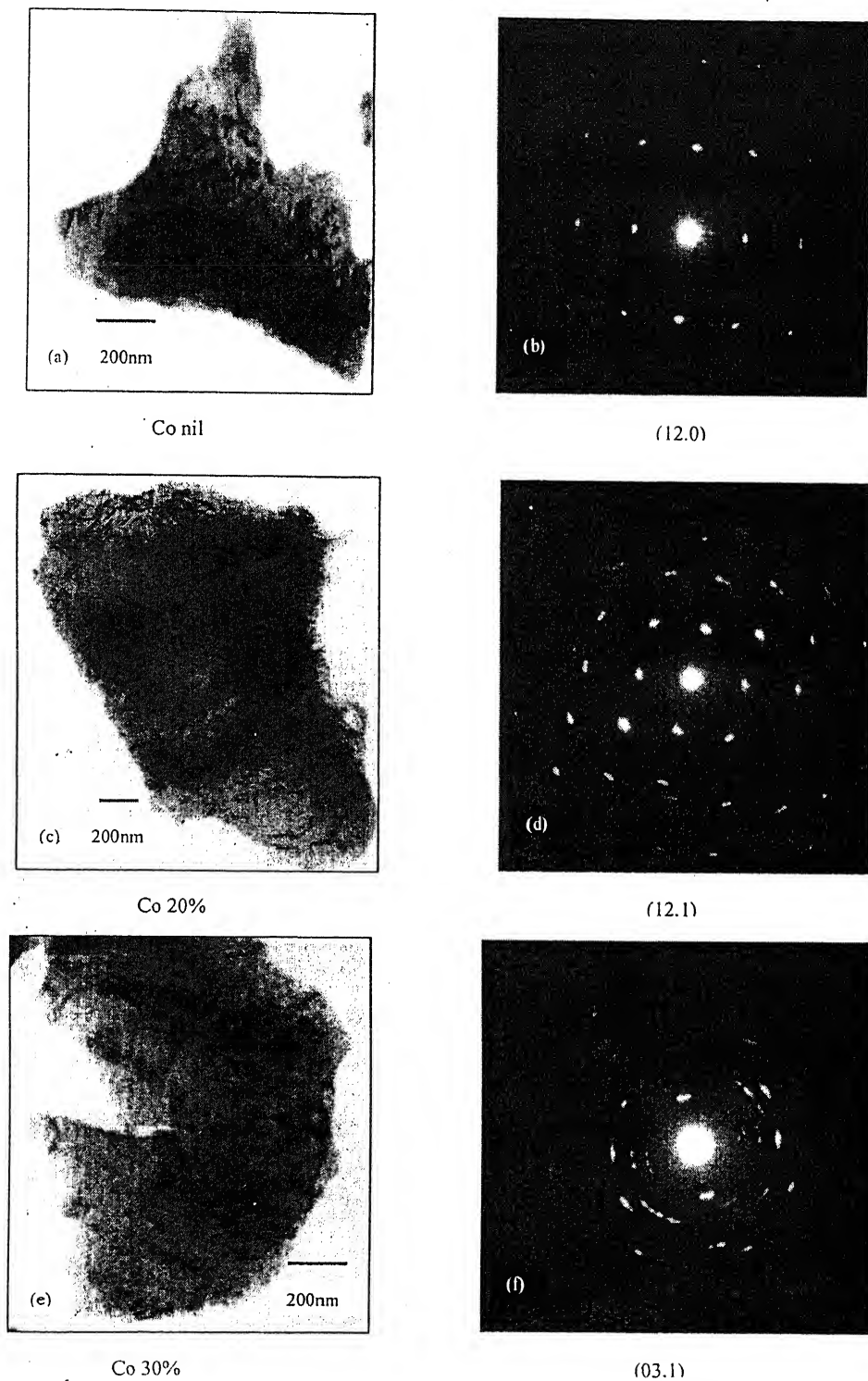


Figure 3.3 Electron micrograph and corresponding diffraction patterns of ZnO: (a), (b) without and (c), (d), (e), (f) with doping of Cobalt

just on the boundary line of the two extreme cases. Figure 3.4(a) and (b) show the temperature dependence of the FC moment as well as the ZFC moment measured at 500 Oe over the temperature range of 10 K to 350 K.

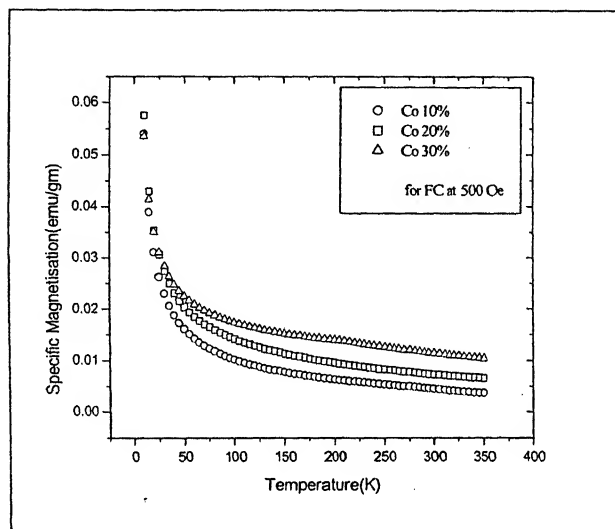


Figure 3.4(a) Specific Magnetization as a function of Temperature for FC case

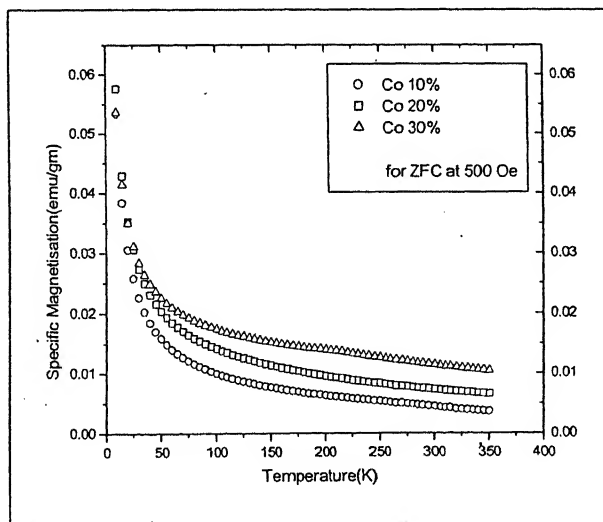


Figure 3.4(b) Specific Magnetization as a function of Temperature for ZFC case

As expected, the sample with highest cobalt concentration displays the greatest specific magnetization. Interestingly however, there is no difference in the FC and ZFC branches of magnetization of the three samples. In a magnetic system, where the moments are frustrated or in an ordered system with pinning, the FC and ZFC branches of the  $M$  vs.  $T$  curves separate out below a critical temperature. The absence of such a separation in these samples clearly indicates the absence of any of the above-mentioned processes.

In the composition range where all cobalt atoms replace Zn sites in the wurtzite lattice, each  $\text{Co}^{2+}$  ion is surrounded by four oxygen ions situated at the corners of a tetrahedron. In the presence of the tetrahedral crystal field, the free ion  $^4F$  ground state splits into a  $^4A_2$  orbital singlet ( $S=3/2$ ), which is the new ground state, and two orbital triplets located at much higher energies [38]. At very dilute concentrations of the  $\text{Co}^{2+}$  ions, the high temperature susceptibility of the systems is expected to follow the Curie-Weiss law. As the  $\text{Co}^{2+}$  concentration increases, exchange interactions between nearest neighbor and higher coordination shell Co ions become relevant. If all these exchange interactions are represented by  $J$ , then at  $k_B T > J$ , the exchange interactions can be incorporated in the susceptibility by using the mean field approximation [39]. The magnetic susceptibility is then expressed in terms of the Curie-Weiss law,

$$\chi = C_0 / (T - T_0)$$

where  $\chi$  is the susceptibility in units of  $\text{emu/g Oe}$ ,  $C_0$  the Curie constant, and  $T_0$ , the Curie-Weiss temperature. The Curie-Weiss fits for three different concentrations at high temperature range of 100-300K are shown in Figure 3.4(c). These fits help in evaluating  $C_0$  and  $T_0$ .

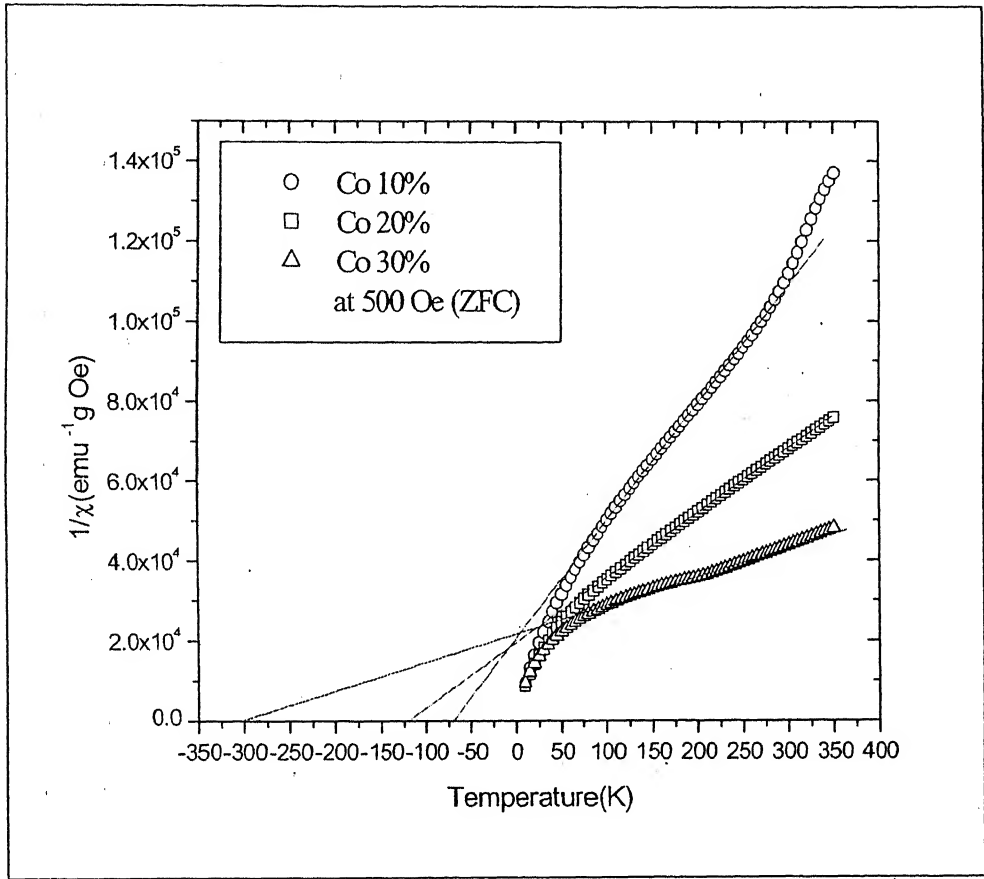


Figure 3.4(c) High Temperature Curie-Weiss fits for  $x=0.10, 0.20$  and  $0.30$

Assuming that only Co ions contribute to magnetic susceptibility, the effective number of Bohr magnetons per cobalt site,  $\mu_{\text{eff}}$  is related to  $C_o$  as;  $\mu_{\text{eff}} = [(3k_B C_o)/N]^{1/2}$  where  $N$  is the Co atoms/gm and  $k_B$  is the Boltzmann constant.

Further, assumption of a complete quenching of the orbital angular momentum of d-electrons in Co ions and taking  $S = 3/2$  allows us to infer the effective gyromagnetic factor as:

$$\mu_{\text{eff}} = g_{\text{eff}} [S(S+1)]^{1/2}.$$

The Curie-Weiss temperature  $T_0$  is also related to the exchange integral  $J$  which derives contributions from the nearest neighbors as well as the second and higher order neighbors;  $J = 3k_B T_0 / S(S+1)$ . The values of  $\mu_{\text{eff}}$ ,  $C_0$  and  $T_0$  extracted from the high temperature linear behavior of  $1/\chi$  (see Fig.3.5(c)) are plotted in Figure 3.4(d) as a function of  $x$ .

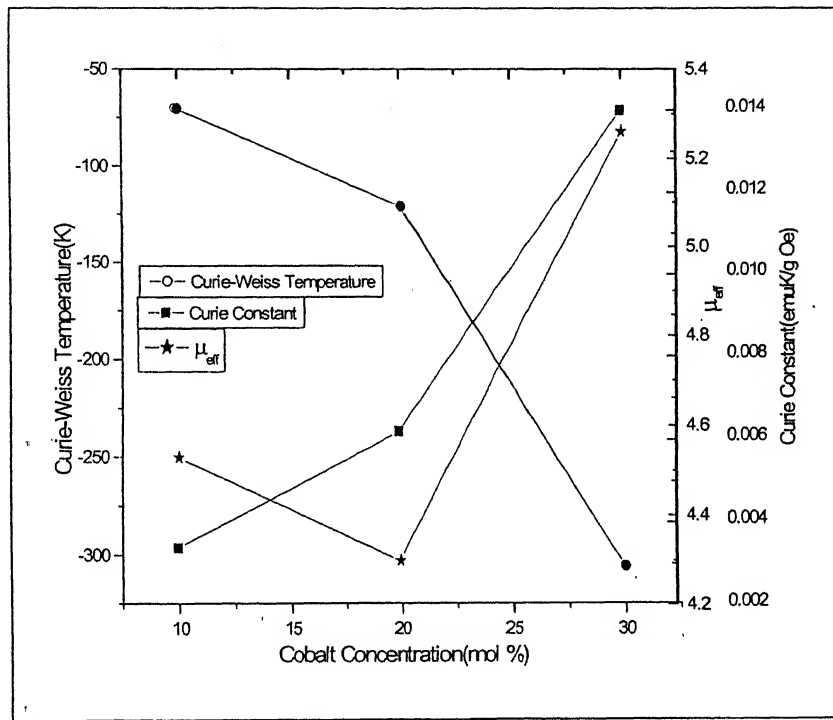


Figure 3.4(d) Curie-Weiss Temperature, Curie Constant and  $\mu_{\text{eff}}$  as a function of Co concentration

We note that in the composition range where a complete solubility of Co is observed in the wurtzite lattice of ZnO, the  $\mu_{\text{eff}}$  is close to 4.4. This leads to a value of  $g_{\text{eff}} \sim 2.2$  only when we have assumed  $S=3/2$ .

The observed negative value of  $J$  (Figure 3.4(e)) signifies an antiferromagnetic

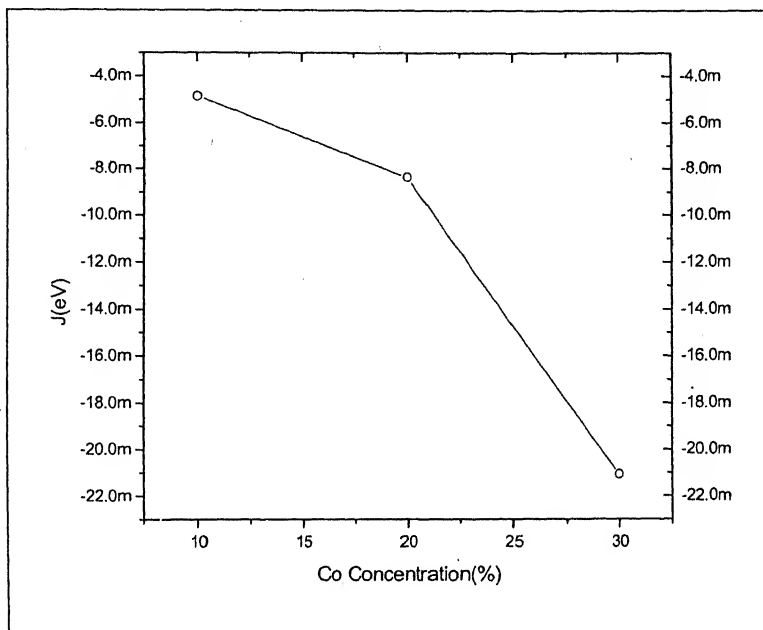


Figure 3.4(e) Variation of exchange integral  $J$  with Co concentration

superexchange between the  $\text{Co}^{2+}$  ions in our samples, as predicted by the theory.

The magnitude of  $J$  is proportional to cobalt doping which represents a strengthening of the antiferromagnetic coupling. It is evident that electron doping at the level of 1 % Al, which means one electron per 10 cobalt atom in  $x = 0.1$  sample, is not enough to surmount the antiferromagnetic superexchange between the Co sites. An increase in doping beyond 1 percent, however, may be difficult to realize. An alternative method to increase the electron concentration is to prepare the samples in highly reducing conditions. The oxygen vacancies thus produced may lead to additional n-type doping.

### 3.5 SUMMARY

We observe substitutional solubility of Co in the wurtzite lattice of ZnO limited to 20 percent at room temperature. A further increase in the cobalt concentration leads to precipitation of cubic CoO and cubic  $\text{Co}_3\text{O}_4$  phases. Electron microscopy done on



several selected areas of the samples did not reveal any second phase though it could have been detected on even more detailed examination as the sample with  $x = 0.30$  had shown clear signs of phase segregation in XRD. We have addressed the issue of mobile carrier assisted ferromagnetism in bulk samples of  $\text{Zn}_{1-x}\text{Co}_x\text{O}$ . Electron carriers were introduced by doping the compound with one mole percent of  $\text{Al}_2\text{O}_3$ . Magnetic measurements show that these materials are paramagnetic down to 10 K with signatures of antiferromagnetic super exchange between the cobalt ions.

## CHAPTER 4

### STRUCTURAL AND OPTICAL

### PROPERTIES OF THIN FILMS

---

#### 4.1 INTRODUCTION

Having discussed the structure and magnetic properties of bulk samples of

$(\text{Zn}_{1-x}\text{Co}_x\text{O})_{99}(\text{Al}_2\text{O}_3)_1$ , we now move on to detailed studies of epitaxial thin films of this Dilute Magnetic Semiconductor. We have synthesized thin films with  $x$  varying from 0.0 to 0.30 in steps of 0.05. These films of thickness ranging from 250 nm to 500 nm were deposited on (00.1) sapphire substrates. This chapter focuses on the structural and optical properties of these films.

#### 4.2 STRUCTURAL CHARACTERIZATION

The X-ray  $\theta - 2\theta$  diffraction patterns of thin films for all values of  $x$  are shown in Figure 4.2(a). The sapphire (00.1) substrate on which the films were deposited acted as the “standard” with which corrections could be made in order to evaluate the lattice constant  $c$ . From the XRD data for thin films, it is evident that all films are highly  $c$ -axis oriented. Two major reflections obtained from the films were (00.2) and (00.4) which correspond to the hexagonal wurtzite structure of ZnO. No Bragg reflections corresponding to an impurity

phase were seen. Since the data in Figure 4.2(a) are plotted on a log scale, the sensitivity of this measurement to detect impurity phases is very good.

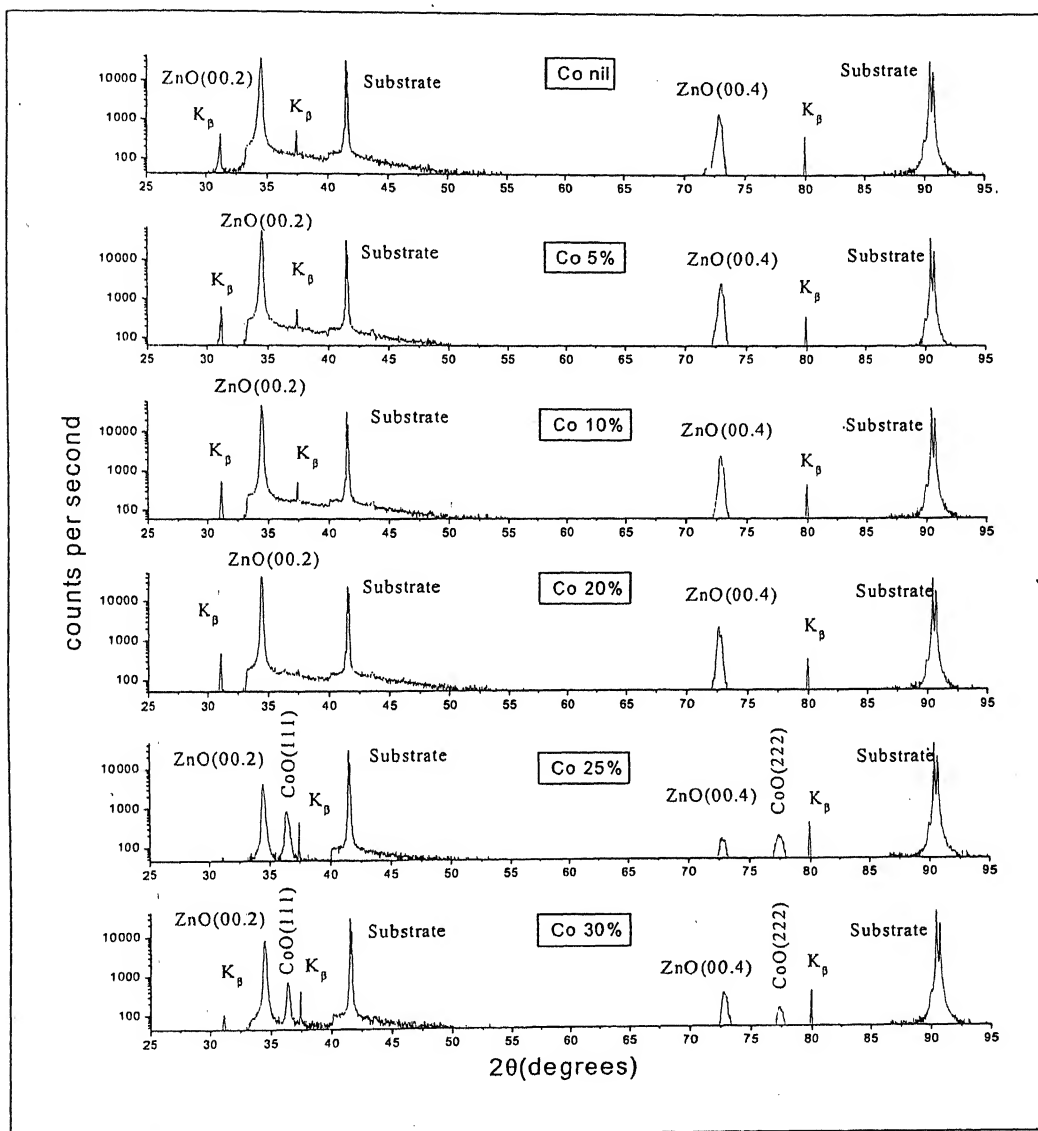


Figure 4.2(a) XRD pattern for thin films with  $x = 0, 0.05, 0.10, 0.20, 0.25$  and  $0.30$ . All the ZnO peaks, substrate peaks and "second" phase peaks have been indexed

The XRD patterns of the samples with  $x > 0.20$ , however, show two additional peaks. These two peaks indicating phase segregation correspond to the cubic phase of CoO: (111) and

(222), in confirmation with the results obtained by Kim et al [18]. Thus, the maximum solubility of Co in ZnO grown on sapphire (00.1) lattice is 20 percent at room temperature grown under a vacuum of  $\sim 10^{-5}$  Torr at a temperature of 600°C.

From the thin film data, the c-axis lattice parameter [derived from d (00.2)] values was calculated and has been plotted as a function of the Co concentration in Figure 4.2(b). The lattice constant  $c$  was found to increase almost linearly till  $x = 0.20$  but after phase segregation, it shows a deviation and saturates with increasing Co content. It is important to mention here some error arising due to the different film thickness for the last two values of  $x$  as the lattice constant is expected to vary with the thickness of the film as well.

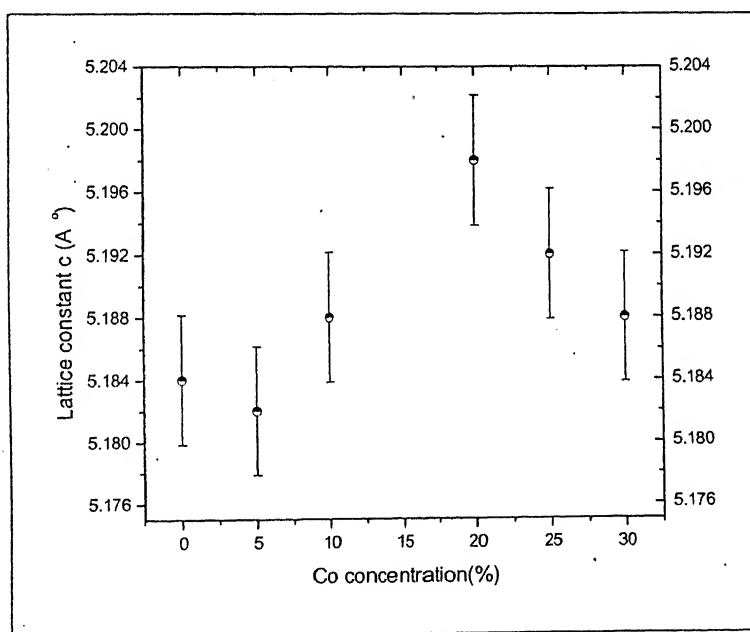


Figure 4.2(b) Variation of lattice constant with Co concentration

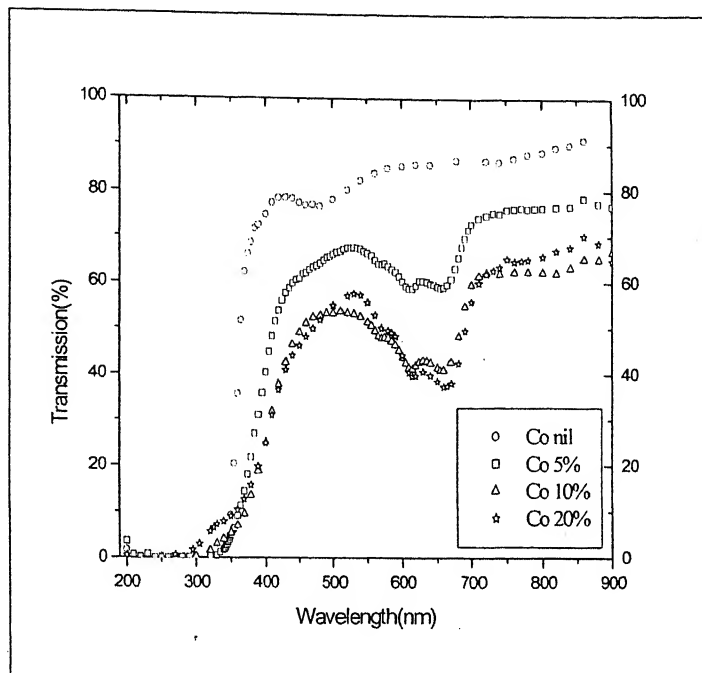
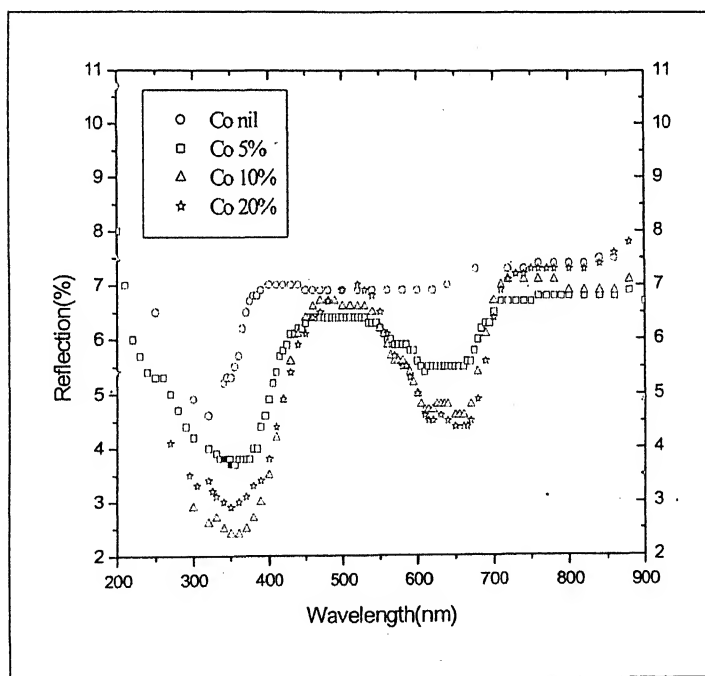
### 4.3 OPTICAL PROPERTIES

In Figure 4.3(a) and 4.3(b), we show the optical transmission and reflectance of the samples with  $x \leq 0.20$  over a wavelength range of 200 nm to 900 nm. The two most important features

of the transmission spectra are that (1), the films are almost transparent ( $\sim 90\%$ ) in the visible regime, and (2), there is presence of certain absorption bands below the fundamental absorption edge. This transparency decreases as we increase the Co content i.e. Co is found to block the transmission of light through the films due to absorption of light in the visible regime. The reflection spectra mostly depict the interference effects.

From the XRD data, it is clear that till  $x = 0.20$ , all the Co goes inside the ZnO lattice without disturbing the hexagonal wurtzite structure i.e.  $\text{Co}^{2+}$  uniformly substitute  $\text{Zn}^{2+}$ . This implies that the substituting  $\text{Co}^{2+}$ , now come under the influence of the tetrahedral field of the oxygen ions (as  $\text{Zn}^{2+}$  originally had been) and as such they will show splitting under their field known as “Tetrahedral Crystal Splitting”. The ground state of the  $\text{Co}^{2+}$  has 7 d electrons. In a free ion ground state, where these electrons have the same energy, the state is designated as  $^4F$  (where the superscript refers to the spin multiplicity,  $2S+1$ ). The tetrahedral crystal field leads to a fine structure of these levels. The number and types of the components into which a tetrahedral field splits up a given L state is the same regardless of the  $d^n$  configuration from which it arises, and these are summarized below:

States in the crystal field	State of free ion
S	$A_1$
P	$T_1$
D	$E + T_2$
F	$A_2 + T_1 + T_2$
G	$A_1 + E + T_1 + T_2$

Figure 4.3(a) Transmission Spectra for  $x = 0, 0.05, 0.10$  and  $0.20$ Figure 4.3(b) Reflectance spectra for  $x = 0, 0.05, 0.10$  and  $0.20$

The symbols used to designate states in the crystal field are called Mulliken's symbols. "A" designates a single degenerate state, "E" designates doubly degenerate states and "T" indicates triple degeneracy. The energy level diagram for  $\text{Co}^{2+}$  free ion and the splitting in presence of tetrahedral crystal field is shown in Figure 4.3(c).

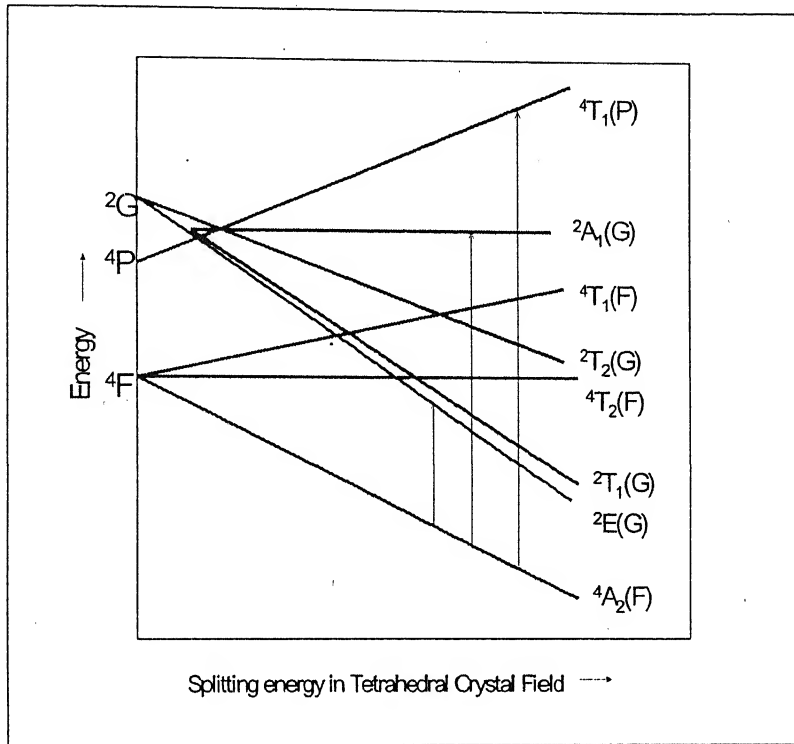


Figure 4.3(c) Splitting of 3d levels of  $\text{Co}^{2+}$  in presence of tetrahedral crystal field

At around  $\sim 2$  eV i.e. in the visible regime, (shown in Figure 4.3(d)), certain absorption bands start appearing. The strength of these bands increases with the Co concentration. Kim et al [30] and Jin et al [3] have interpreted that these absorption bands are due to the transitions involving crystal field split 3d levels in  $\text{Co}^{2+}$  ions substituting  $\text{Zn}^{2+}$  ions as shown in Figure 4.3(c). The three absorption bands which are clearly resolved in all three cases of Co doping

have been assigned as due to  $^4A_2(F) \rightarrow ^2E(G)$ ,  $^4A_2(F) \rightarrow ^4T_1(P)$ , and  $^4A_2(F) \rightarrow ^2A_1(G)$  at energies  $\sim 1.89$  eV,  $\sim 2.02$  eV and  $\sim 2.18$  eV respectively. As these absorption bands correspond to red color of the EM spectrum, perhaps this could be the reason for the films being blue-green in color [5].

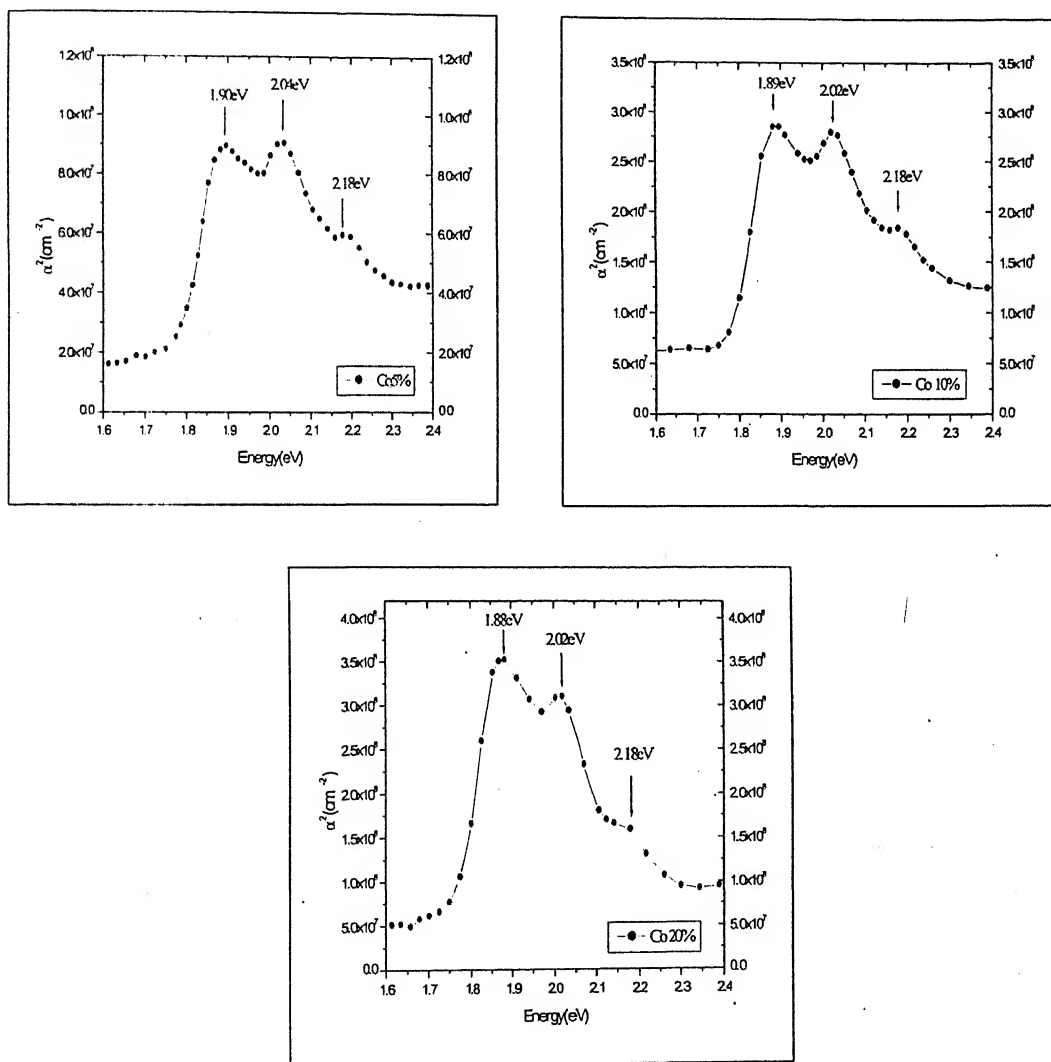


Figure 4.3 (d) Magnified views of the absorption bands observed for all three values of x



Plots of  $\alpha^2$  as a function of energy (eV) for all values of  $x$  are shown in Figure 4.3(e).

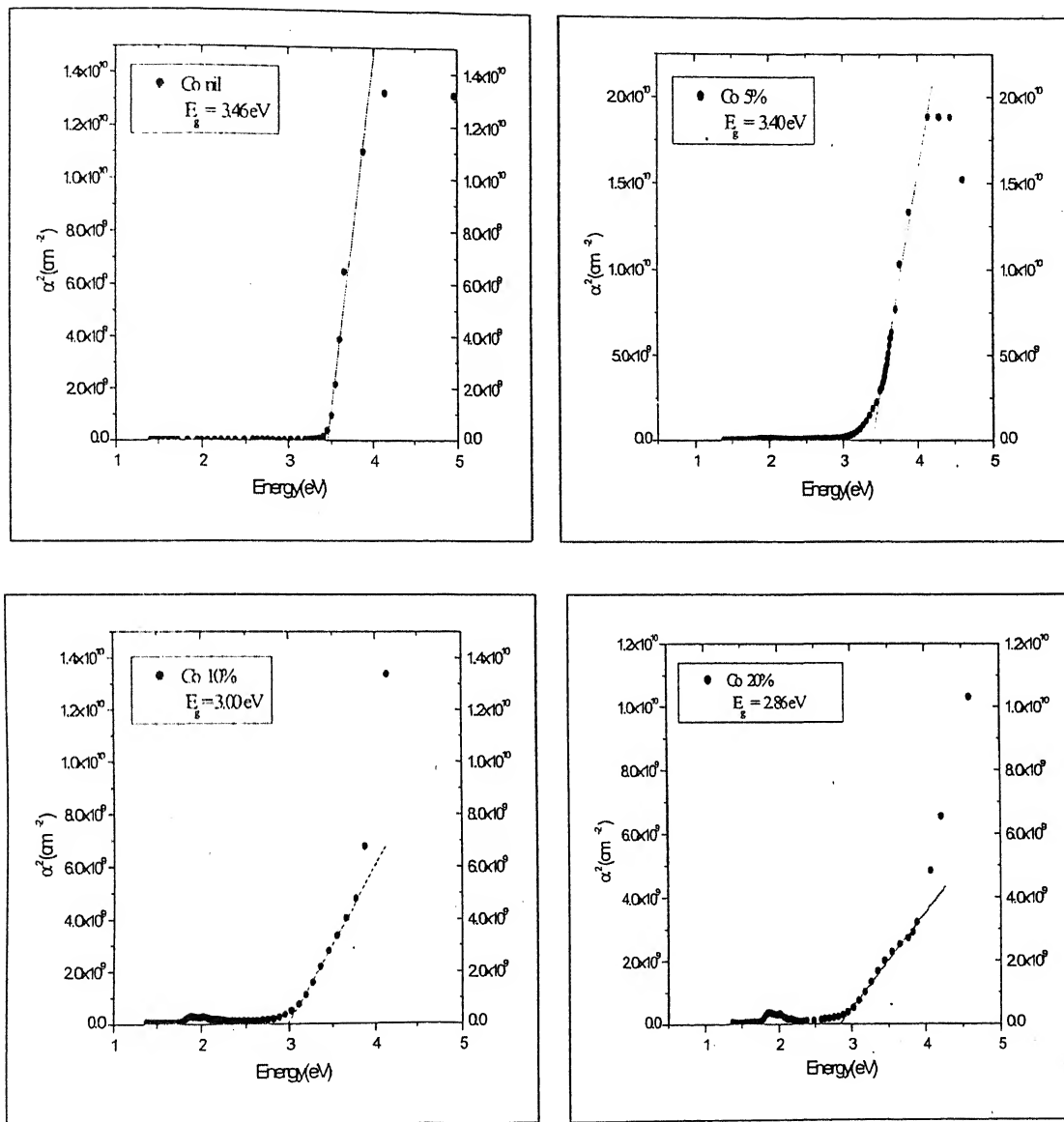


Figure 4.3(e)  $\alpha^2$  as a function of energy in eV

Band gap calculated, as discussed earlier, for each composition and its variation with Co concentration has been plotted as shown in Figure 4.3 (f).

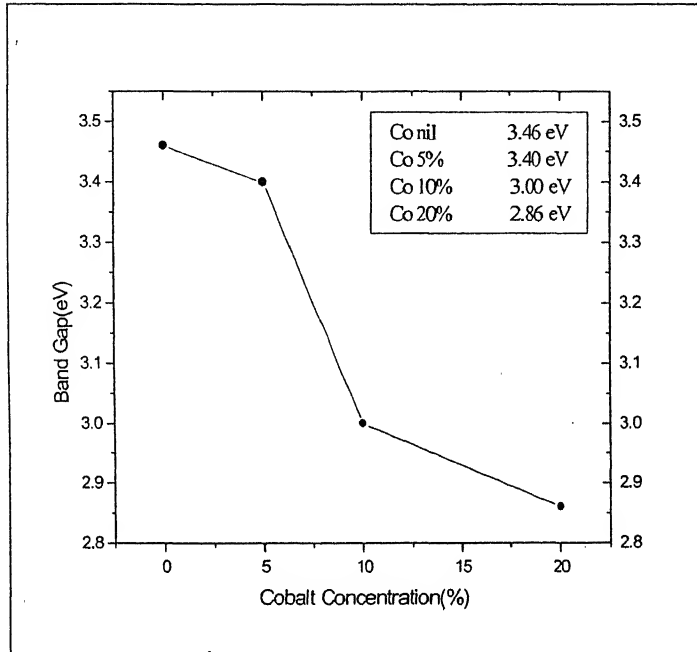


Figure 4.3(f) Red shift of the optical band edge with increase in Co concentration

The carrier concentration in our samples at 200K is  $\sim 10^{20}$ . It is well beyond the Mott minimum carrier concentration for an insulator – to – metal transition in a doped semiconductor. Thus, we have an n-type highly degenerate semiconductor. The energy gap of a semiconductor undergoes a change on doping. The magnitude of the shift is decided by two competing mechanisms. There is a band-gap widening due to the Burstein-Moss shift [40] given by

$$E_g = E_{g0} + \Delta E_{B-M}$$

where  $E_{g0}$  is the intrinsic band gap ( $\sim 3.37$  eV) and  $\Delta E_{B-M}$  is the B-M shift. This shift is calculated assuming both the conduction and valence bands to be parabolic and is found to be proportional to the carrier concentration as  $n^{2/3}$ . The second mechanism, which comes into

play at such high carrier densities, is due to a change in the nature and strength of the interaction potentials between the donors and the host crystal. This gives rise to band gap shrinkage [41] and to some increased tailing of the absorption edge. The shrinkage has been found to be proportional to  $n^{1/3}$  based on a weakly interacting electron gas model for n-Ge and p-GaAs. [26]. However, ZnO along with Si: P and Si-As do not follow this dependence.

As stated earlier, all compositions have 1 molar% doping of  $\text{Al}_2\text{O}_3$  and hence have an electron density well above the Mott critical density. Thus, the band gap widening effect due to B-M shift would be uniform for all samples. The shift is best reflected in the sample, which has no Co doping. The  $E_g$  calculated for that sample is 3.46 eV, which is 90meV higher than that for pure ZnO. However, introduction of Co into the ZnO lattice is found to cause a red shift of the band gap unlike the case of Co doped  $\text{TiO}_2$  [32] or Mn doped ZnO [22] where a blue shift has been observed. The narrowing has been as large as 600 meV for  $x = 0.20$  as compared to the sample with  $x = 0$  where  $x$  represents the Co content. But Co doping also suppresses the carrier concentration as has been observed by our Hall data. So none of the current models that are all based on narrowing of band gap being proportional to the carrier concentration is able to explain the narrowing observed by us. Kim et al have observed a similar narrowing in Co-doped ZnO samples deposited by rf magnetron sputtering. They have attributed this narrowing to the sp-d exchange interactions between the band electrons and the localized d electrons of the  $\text{Co}^{2+}$  ions substituting the host  $\text{Zn}^{2+}$  ions.

#### 4.4 SUMMARY

The thin films deposited by PLD in pressure  $\sim 10^{-6}$  Torr at 600 °C are found to be highly c-axis oriented. We have found that the maximum solubility of  $\text{Co}^{2+}$  in ZnO lattice at room temperature is 20 percent. At concentrations higher than this, there are clear signs of phase

segregation in form of cubic CoO. The lattice constant is found to increase with increasing Co content. Our films have been found to be almost transparent in the visible regime with certain absorption bands near  $\sim 2$  eV, arising due to the transitions between split d-levels of  $\text{Co}^{2+}$  substituting  $\text{Zn}^{2+}$  in presence of tetrahedral crystal field of the oxygen ions. Direct band gap has been found to show a red shift with increasing Co doping.

गुरुप्राप्तम काशीनाथ कलकर पुस्तकालय  
भारतीय प्रौद्योगिकी संस्थान कानपुर  
अवधि क्र० A . 149266

## CHAPTER 5

# TRANSPORT AND MAGNETIC PROPERTIES OF THIN FILMS

---

### 5.1 INTRODUCTION

In this chapter, we shall discuss the transport and magnetic properties of thin film samples. Transport properties would include resistivity and Hall Effect measurements, which are important to evaluate parameters like majority carrier concentration and their Hall mobility. Study of magnetic properties would include Magnetization vs. Temperature (M-T) and Magnetization vs. Field (M-H) measurements. These are important to understand the interaction between the donor electrons and the localized d electron moments at  $\text{Co}^{2+}$  sites.

### 5.2 TRANSPORT PROPERTIES

Figure 5.2(a) shows the variation of the room temperature resistivity with Co concentration. While the resistivity for the Co free sample is quite low ( $\sim 1$  mohm -cm), it increases on substitution of Co. In the regime of complete solubility, this enhancement in  $\rho$  (300K) can be attributed to the s-d scattering. The increase in  $\rho$  (300K) with  $x$  is much sharper for  $x > 0.20$ . This is presumably an effect of the two-

phase nature of the film.  $\rho(T)$  plots of the samples with  $x = 0, 0.05, 0.10, 0.20$  and  $0.30$  are shown in Figure 5.2(b). It is important to note that the resistivity of the sample with  $x = 0$  is metallic ( $d\rho / dT$  is positive) throughout the temperature range. The relatively small magnitude and the metallic temperature dependence of the resistivity of the cobalt- free sample are characteristics of a heavily degenerate semiconductor.

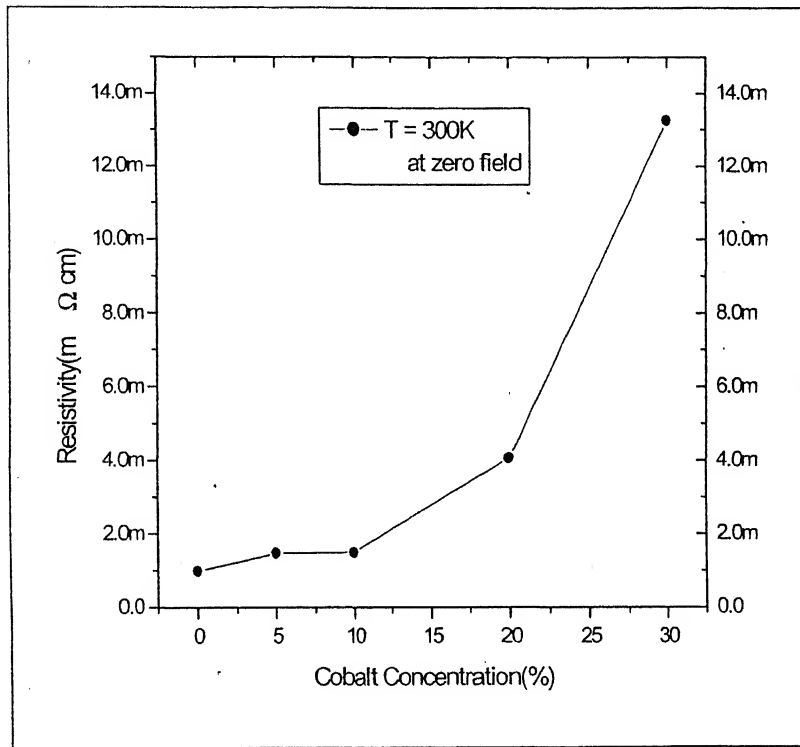


Figure 5.2(a) Variation of room temperature resistivity with Co concentration

The critical carrier density required for insulator to metal transition in a doped semiconductor is given by:

$n_{IM} = [0.25 / a^*]^3$  where  $a^*$  is the donor radius and is given by

$$a^* = \epsilon \hbar^2 / m^* e^2$$

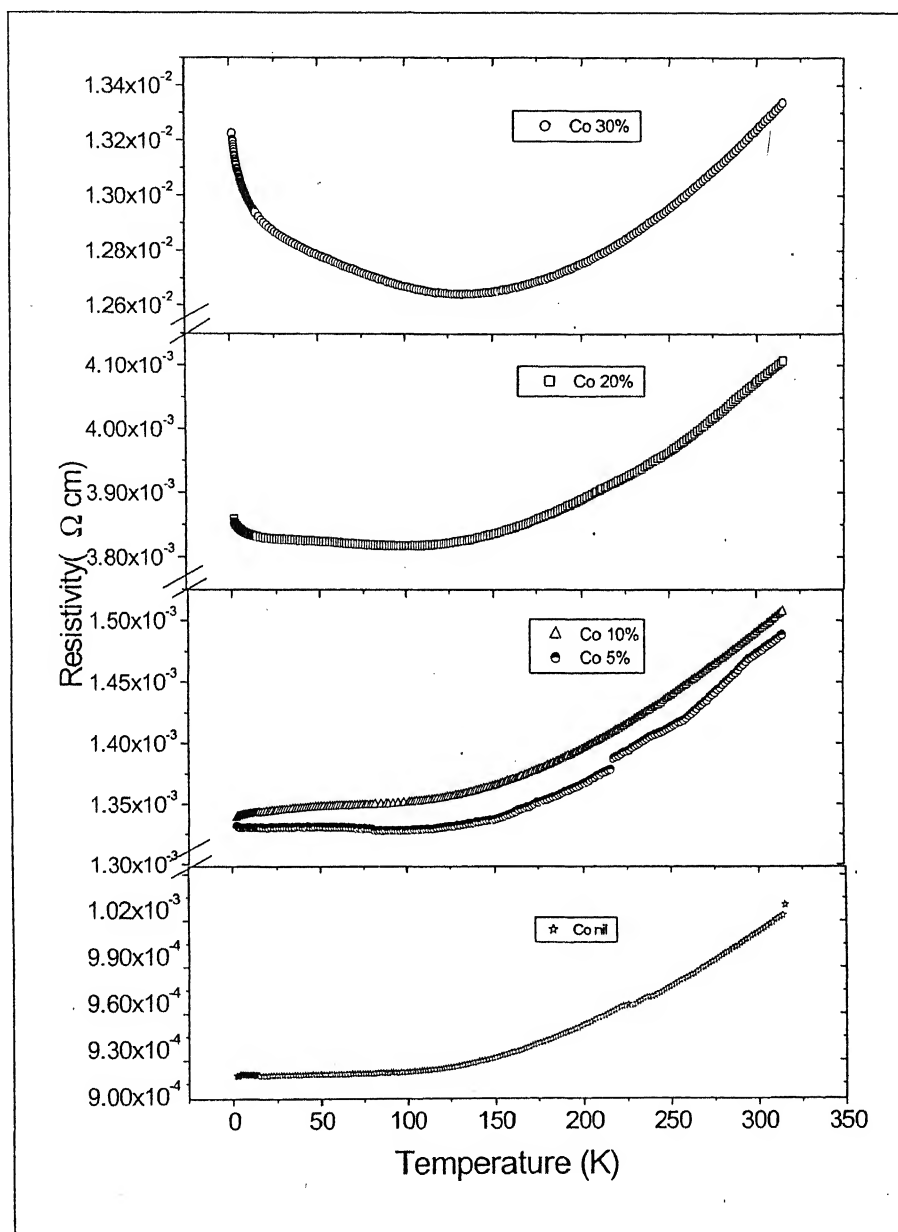


Figure 5.2(b) Variation of resistivity with temperature for all values of  $x$  ranging from 0 to 0.30

where  $m^*$  is the electron effective mass and  $\epsilon$  the dielectric constant for the material. Using  $m^* = 0.38m$  and  $\epsilon = 8.5$  for ZnO, the donor radius is  $\sim 11.8 \text{ \AA}$ . With this  $a^*$ , we get  $n_{IM}$  as  $9.4 \times 10^{18} / \text{cm}^3$ . The measured carrier concentration in the Co free sample is much higher than this number. Clearly we have a heavily degenerate semiconductor whose Fermi level is in the conduction band. Figure 5.2 (c) and (d) sums up the transport measurements as it depicts the temperature dependence of the carrier concentration as well as the Hall mobility for all values of  $x$  ranging from 0 to 0.30. The carrier concentration shows a small but distinct increase with temperature. The Hall mobility drops by a factor of  $\sim 4$  on increasing the concentration from  $x = 0$  to  $x = 0.30$ . The carrier concentration is also found to be suppressed with the increase in the amount of Co doping.

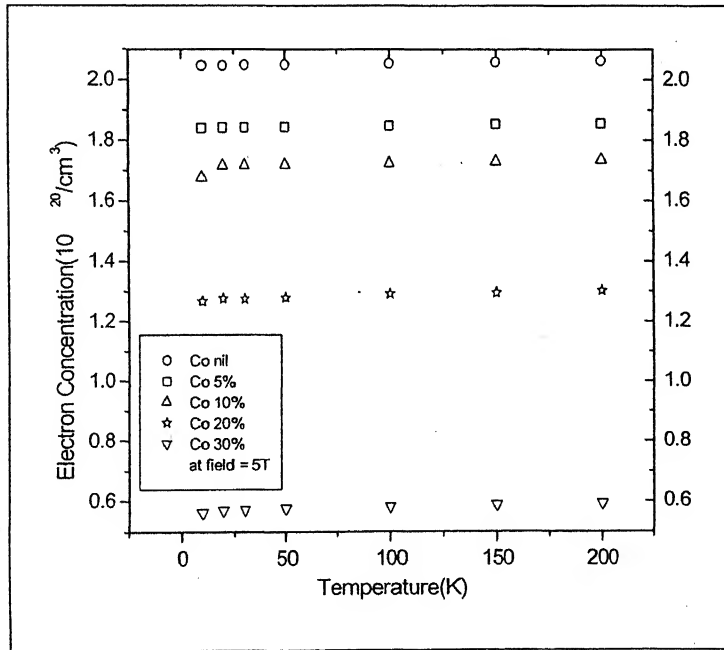


Figure 5.2(c) Variation of electron concentration with temperature for all values of  $x$



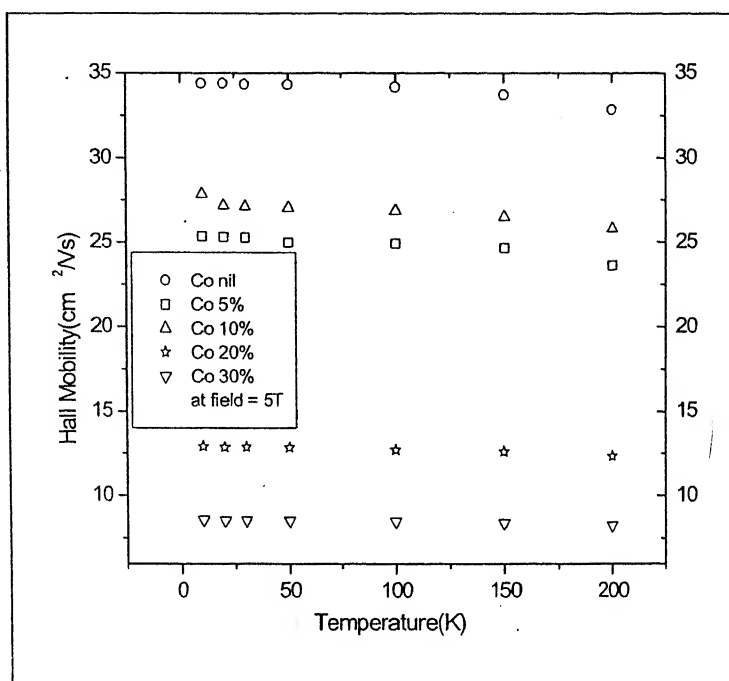


Figure 5.2(d) Variation of Hall mobility with temperature for all values of  $x$

Since all the samples have a uniform doping of  $\text{Al}_2\text{O}_3$ , it can be inferred that Co is in some way responsible for either trapping the mobile charge carriers or scattering them.

### 5.3 MAGNETIC PROPERTIES

We have studied the magnetic properties in terms of Magnetization vs. Temperature (M-T) and Magnetization vs. Field (M-H) measurements. Figure 5.3(a) and (b) depict the M-H curves for  $x = 0.20$  and  $0.30$  samples, they show clear signs of hysteresis at 10K. However, the hysteresis has a negligible remanant magnetization. This is indicative of a superparamagnetic behavior. However, a word of caution is necessary while interpreting magnetization data on thin film samples. To illustrate this point, in Figure 5.3(c), we show the M-H curve of a bare sapphire substrate.

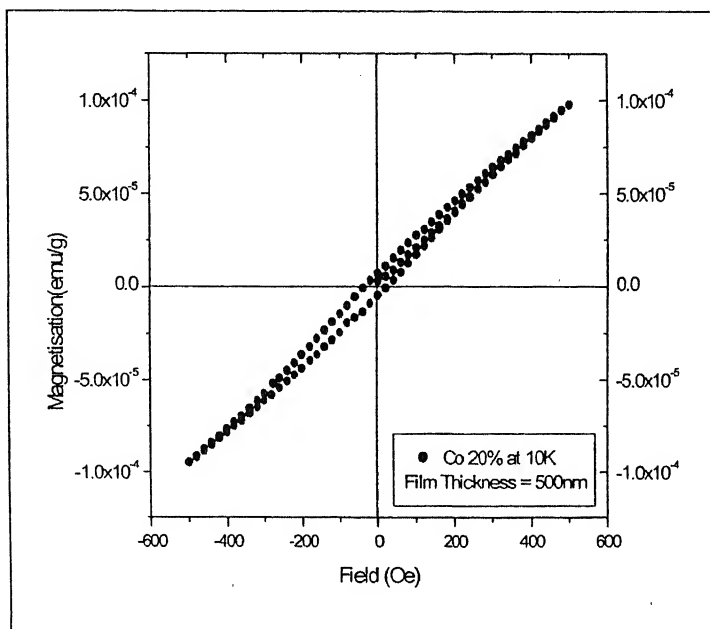
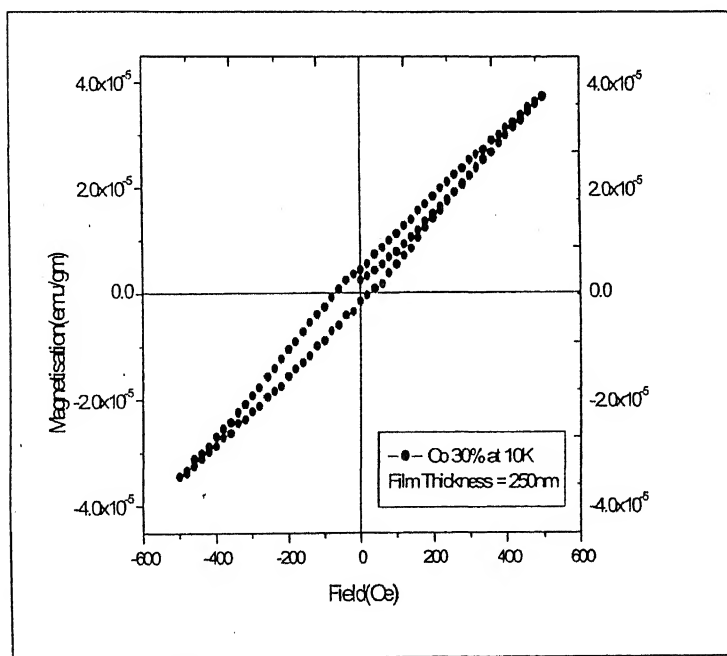
Figure 5.3(a) M-H curve for  $x = 0.20$  at 10K

Figure 5.3(b) M-H curve for 0.30 at 10K

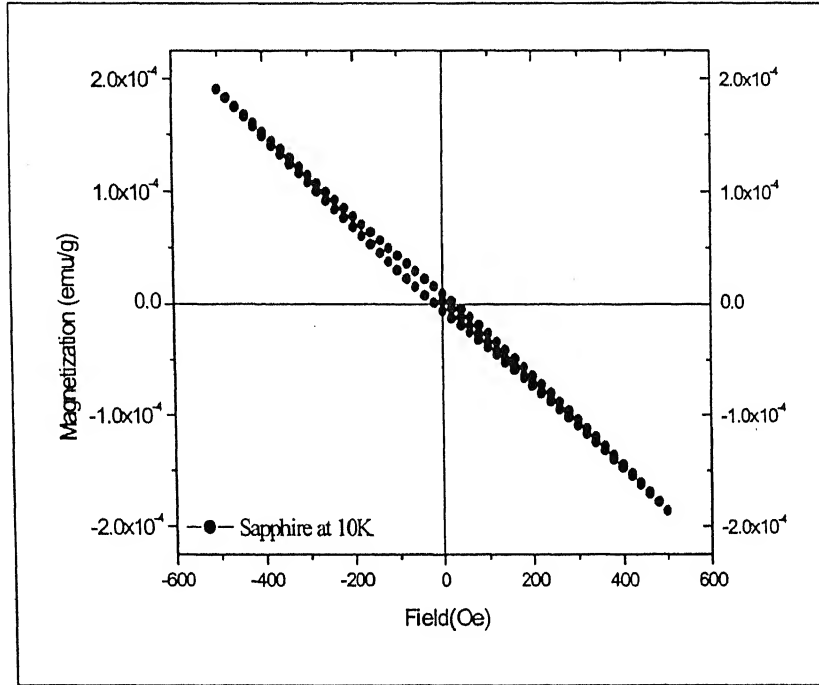
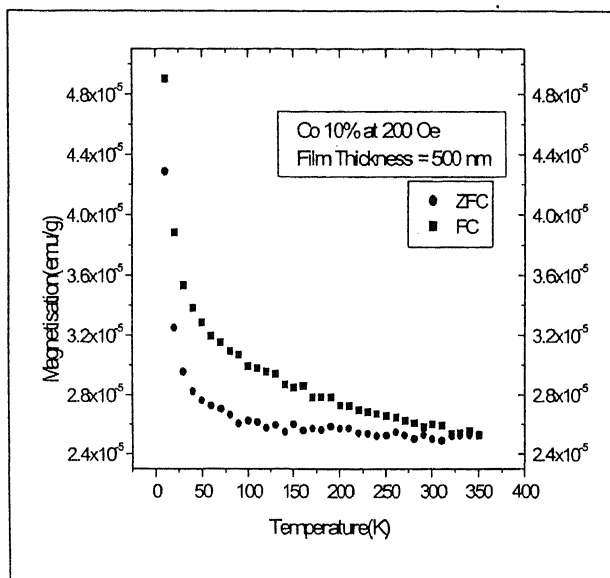
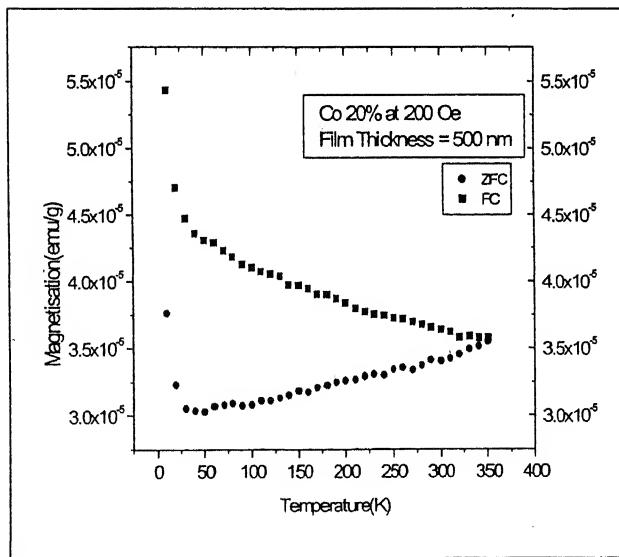


Figure 5.3(c) M-H curve for sapphire at 10K

The diamagnetic response of the substrate is almost of the same order of magnitude for  $x = 0.20$  and  $\sim 5$  times larger than the response of the film for  $x = 0.30$ . The magnetization data on thin films, therefore, have a large error.

More information can be retrieved about the magnetic state of the samples from the MT curves as shown in Figure 5.3(d), (e) and (f). The magnetization curve for  $x = 0.10$  is paramagnetic though the Zero Field Cooled (ZFC) and Field Cooled (FC) moments differ in magnitude. However, the curves for  $x=0.20$  and  $0.30$  show behavior characteristic to that for superparamagnetism. [41]. The discrepancy between the ZFC and FC curves is all the more visible in case of  $x=0.30$ . As the measurements have been done at 200 Oe, the blocking temperature ( $T_B$ ) is of the order of  $\sim 300\text{K}$  though it

Figure 5.3 (d) M-T curve for  $x = 0.10$  at 200 OeFigure 5.3 (e) M-T curve for  $x = 0.20$  at 200 Oe

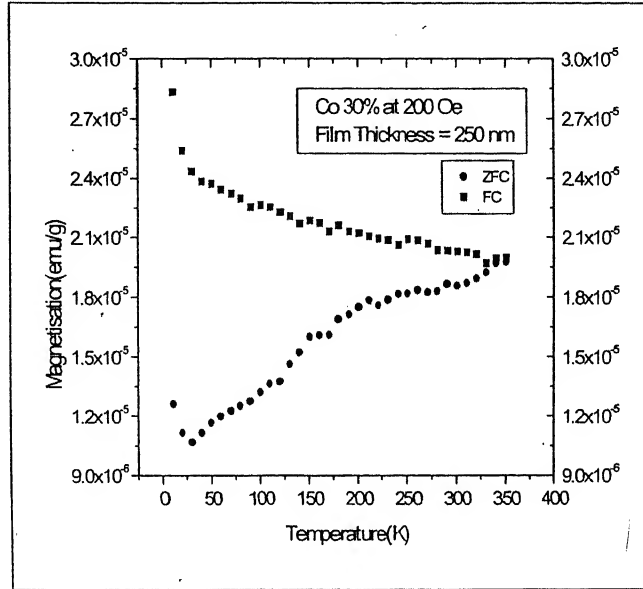


Fig. 5.3 (f) M-T curve for  $x = 0.30$  at 200 Oe

is also dependent on the volume of the superparamagnetic cluster and its anisotropy energy as [42]:

$$T_B \sim K * V / 30k_B$$

Where  $K$  is the magnetic anisotropy energy,  $V$  is the volume of the superparamagnetic cluster and  $k_B$  is the Boltzmann constant. As we increase the field, the blocking temperature is expected to decline, as the increased energy supplied by the field would help in orienting the superparamagnetic moments at lower temperature. Park et al [41] have supported the superparamagnetic behavior in their films prepared by sol-gel technique with TEM studies where the doping concentration of Co exceeds the maximum solubility limit. Their TEM samples reveal the presence of  $\sim 10$  nm sized Co clusters in their samples.

The superparamagnetic behavior seen could well indicate the presence of Co clusters in our samples. These clusters could be too small to be detected by XRD. We further need TEM studies to verify the presence of Co clustering in our samples, if any.

We have also fitted the inverse susceptibility curves at high temperatures for the FC case with Curie-Weiss law shown in Figure 5.3(g) and evaluated the Curie constant as well as the Curie-Weiss temperature for all three concentrations which are tabulated at the end.

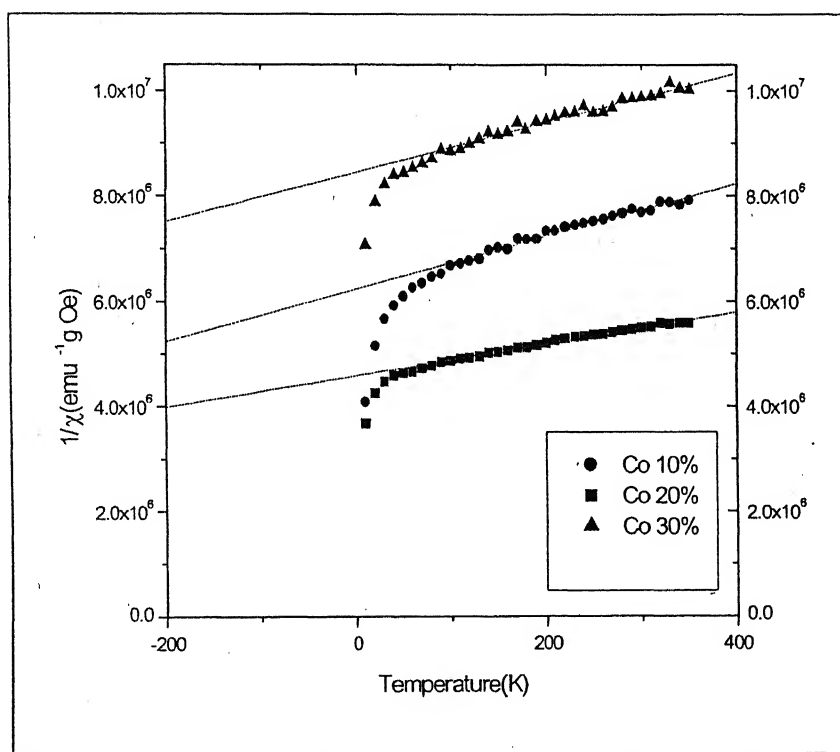


Figure 5.3(g) Curie-Weiss fits at high temperature for  $x = 0.10, 0.20$  and  $0.30$

The negative Curie-Weiss temperature and hence a negative value for the exchange integral  $J = 3 * k_B * T_o / S(S+1)$  clearly indicates that there is anti-ferromagnetic interaction between the nearest neighbor  $Co^{2+}$  in the films as well.  $J$  is of the order of  $\sim 100$  meV and so the interaction in this case is found to be much stronger than in bulk.

Co conc. (%)	Curie Weiss Temp (K)	Curie constant (emu <sup>-1</sup> g Oe K)	Exchange Integral J (meV)
10	-1246.2	1.9E-4	85 meV
20	-1519.3	3.3E-4	104 meV
30	-1793.5	2.1E-4	123 meV

## 5.4 SUMMARY

The room temperature resistivity for all values of  $x$  ranging from  $x = 0$  to  $0.30$  has been measured and it shows a gradual increase till  $x = 0.20$  and an abrupt increase once the maximum solubility limit is crossed. The resistivity of cobalt-free sample is  $\sim 1$  mohm-cm and the films become increasingly resistive with Co doping. Both carrier concentration and Hall mobility are suppressed with increase in Co doping.

The magnetization data has error, as the diamagnetic response of the bare substrate is quite large. However, we have found a paramagnetic state for  $x = 0.10$  and superparamagnetic state for  $x = 0.20$  and  $0.30$  samples with blocking temperature ( $T_B$ ) as high as  $\sim 300$ K. These two compositions have also shown clear signs of hysteresis at  $10$ K although with negligible remnant magnetization, which further supports a superparamagnetic state. The superparamagnetic state indicates formation of Co clusters, which we have to verify by TEM studies in our samples. The Curie-Weiss fits

at high temperature yield a negative value of the exchange integral  $J$  which again indicates an antiferromagnetic interaction between the Co ions though the interaction in this case is found to be much stronger as compared to bulk.



## CONCLUSIONS

1. We have successfully prepared bulk samples and thin epitaxial films of  $\text{Zn}_{1-x}\text{Co}_x\text{O}$  Dilute Magnetic Semiconductor. The maximum solubility limit of  $\text{Co}^{2+}$  into the ZnO lattice is 20 percent both for bulk as well as thin films at room temperature.
2. Transmission Electron Microscopy studies on bulk samples did not reveal any Co clustering even for  $x = 0.30$  where a “second” phase of Co had been detected by XRD. The single crystal micrographs and their corresponding diffraction pattern were found to be those of hexagonal ZnO.
3. The films were found to be highly transparent ( $\sim 90\%$ ) in the visible region of the EM spectrum with certain absorption bands appearing around  $\sim 2$  eV for Co doped samples. These have been attributed to the d-d transitions between the split-levels of  $\text{Co}^{2+}$  in a tetrahedral crystal field. The optical band edge shows a red shift with increase in Co doping.
4. The bulk samples were found to be paramagnetic for  $x = 0.10, 0.20$  and  $0.30$  with antiferromagnetic interaction between the Co ions. The films were paramagnetic for  $x = 0.10$  and superparamagnetic for  $x = 0.20$  and  $x = 0.30$  with blocking temperature ( $T_B$ ) as high as  $\sim 300\text{K}$ . The M-H curves were hysteretic for these two values of  $x$  with negligible remnant magnetization, which further supports a superparamagnetic state. The interaction between Co ions was antiferromagnetic for thin films as well, though much stronger as compared to bulk.
5. The room temperature resistivity shows a gradual increase till  $x = 0.20$  and an

abrupt increase once the maximum solubility limit is crossed. The films become increasingly resistive with Co doping. Both carrier concentration as well as Hall mobility is suppressed by incorporation of Co.

---

## REFERENCES

1. S. A. Wolf, D. D. Awschalom, R. A. Buhrman, J. M. Daughton, S. von Molnar, M. L. Roukes, A. Y. Chtchelkanova, D. M. Treger, *Science*, **294**, 1488, (2001)
2. IBM Journal of Research & Development, S. Methfessel, **14**(3), 207, 1970
3. Zhengwu Jin, T. Fukumura, M. Kawasaki, K. Ando, H. Saito, T. Sekiguchi, Y. Z. Yoo, M. Murakami, Y. Matsumoto, T. Hasegawa and H. Koinuma, *Appl. Phys. Lett.*, **78**(24), 3824, 2001.
4. A. Lewicki, A.I. Schindler, J.K. Furdyna and W. Giriat, *Phys. Rev. B*, **40**(4), 2379, 1989
5. J. K. Furdyna, *J. Appl. Phys.*, **64**(4), R29, 1988
6. W. Prellier, A. Fouchet and B. Mercey, *J. Phys.: Condens. Matter*, **15**, R1583, 2003
7. H. Ohno, *Science*, **281**, 951, 1998
8. T. Dietl, H. Ohno, F. Matsukura, J. Cibert, D. Ferrand, *Science*, **287**, 1019, (2000)
9. K. Saito and H. Katayama-Yoshida, *Physica B*, **308-310**, 904, 2001
10. Yuji Matsumoto, Makato Murakami, Tomoji Shomo, Tetsuya Hasegawa, Tomoteru Fukumura, Masashi Kawasaki, Parhat Ahmet, Toyohiro Chikyow, Shin-ya Koshihara and Hideomi Koinuma, *Science*, **291**, 854
11. S.B. Zhang, S.-H. Wei and Alex Zunger, *Phys. Rev. B*, **63**, 075205 (2001)
12. Chris G. Van de Walle, *Physica B*, **308-310**, 899-903 (2001)
13. J. F. Muth, R. M. Kolbas, A.K. Sharma, S. Oktyabrsky, J. Narayan, *J. Appl. Phys.*, **85**(11), 7884 (1999)

14. H H. Sawada, R. Wang and A. W. Sleight, *J. Solid Stat. Chem.*, **122**, 148, 1996
15. A. Fouchet, W. Prellier, P. Padhan, Ch. Simon, B. Mercey, V. N. Kulkarni and T. Venkatesan, *J. Appl. Phys.*, **95**(11), 7187, 2004
16. A.S. Risbud, N. A. Spaldin, Z.Q.Chen, S.Stemmer, Ram Seshadri, *Phys. Rev. B*, **68**, 205202, (2003)
17. S. Kolesnik, B. Dabrowski,, J. Mais, *J. Appl. Phys*, **95**(5), 2582, (2004)
18. Jae Hyun Kim, Hyojin Kim, Dojin Kim, Young Eon Ihm, Woong Kil Choo, *J. Appl. Phys.*, **92**(10), 6066, (2002)
19. Jae Hyun Kim, Jae Bong Lee, Hyojin Kim, Dojin Kim, Young Eon Ihm, Woong Kil Choo, *IEEE Trans. Mag.*, **38**(5), 2880, (2002)
20. Hyeon-Jun Lee, Se-Young Jeong, Cae Ryong Cho and Chul Hong Park, *Appl. Phys. Lett.*, **81**(21), 4020, 2002
21. Kenji Ueda, Hitoshi Tabata and Tomoji Kawai, *Appl. Phys. Lett.*, **79**(7), 988-990, 2001
22. T. Fukumura, Zhengwu Jin, A. Ohtomo, H. Koinuma and M. Kawasaki, *Appl. Phys. Lett.*, **75**(21), 3366, 1999
23. S.R.Shinde, S.B. Ogale, J. S. Higgins, H. Zheng, A. J. Millis, V. N. Kulkarni, R.Ramesh, R. L. Greene and T. Venkatesan, *Phys. Rev. Lett.*, **92**(16), 166601, 2004
24. S.R.Shinde, S.B. Ogale, S. Das Sarma, J. R. Simpson, H. D. Drew, S.E. Lofland, C. Lanci, J.P. Buban and N. D. Browning, *Phys. Rev. B*, **67**, 115211, 2003

- 
25. S.B. Ogale, R.J. Choudhary, J.P. Buban, S.E. Lofland, S.R. Shinde, S. N. Kale, V. N. Kulkarni, C. Lanci, J. R. Simpson, N. D. Browning, S. Das Sarma, H. D. Drew, R. L. Greene and T. Venkatesan, *Phys. Rev. Lett.*, **91**(7), 077205, 2003
  26. Alain P. Roth, James B. Webb and Digby F. Williams, *Phys. Rev. B*, **25**(12), 7836, 1982
  27. B. E. Sernilius, K. F. Breggren, Z. C. Jin, I. Hamberg and C. G. Granqvist, *Phys. Rev. B*, **37**(17), 10244-10248, 1988
  28. A. V. Singh, Manoj Kumar, R. M. Mehra, Akihiro Wakahara and Akira Yoshida, *J. Indian Inst. Sci.*, **81**, 527-533, 2001
  29. Lata Gupta, Abhai Mansingh and P.K. Srivastava, *Appl. Surface Science*, **33/34**, 898-904, 1988
  30. Kwang Joo Kim and Young Ran Park, *Appl. Phys. Lett.*, **81**(8), 1420-1422, 2002
  31. Y. Z. Yoo, T. Fukumura, Zhengwu Jin, K. Hasegawa, M. Kawasaki, P. Ahmet, T. Chikyow and H. Koinuma, *J. Appl. Phys.*, **90**(8), 4246-4250, 2001
  32. J. R. Simpson, H. D. Drew, S. R. Shinde, R.J. Choudhary, S. R. Ogale and T. Venkatesan, *Phys. Rev. B*, **69**, 193205, 2004
  33. Kyoung-Kook Kim, Hyun-Sik Kim, Dae-Kue Hwang, Jae-Hong Lim and Seong-Ju Park, *Appl. Phys. Lett.*, **83**(1), 63-65, 2003
  34. J. F. Rommeluere, L. Svob, F. Jomard, J. Mimila-Arroyo, A. Lusson, V. Sallet and Y. Marfaing, *Appl. Phys. Lett.*, **83**(2), 287, 2003
  35. C. Marcel, N. Naghavi, G. Couturier, J. Salardenne and J. M. Tarascon, *J. Appl. Phys.*, **91**(7), 4291, 2002

- 36. Nicola A. Spaldin, Phys. Rev. B, **69**, 125201, 2004
- 37. Eun-Cheol, K.J. Chang, Phys. Rev. B, **69**, 085205, 2004
- 38. A. Lewicki, A. I. Schindler, I. Miotkowski and J. K. Furdyna, Phys. Rev. B, **41**(7), 4653, 1990
- 39. J. Spalek, A. Lewicki, Z. Tarnawski, J. K. Furdyna, R. R. Galazka and Z. Obuszko, Phys. Rev. B, **33**(5), 3407, 1986
- 40. I. Hamberg, C. G. Granqvist, K.-F. Breggren, B. E. Sernilius and L. Engstrom, Phys. Rev. B, **30**(6), 3240, 1984
- 41. Jung H. Park, Min G. Kim, Hyun M. Jang, Sangwoo Ryu and Young M. Kim, Appl. Phys. Letter, **84**(5), 1338, 2004
- 42. D. H. Kim, J. S. Yang, Y. S. Kim, D. -W. Kim, T. W. Noh, Y. -W. Kim, Y. D. Park, Y. Jo and J.- G. Park, Appl. Phys. Lett., **83**(22), 4574, 2003